Article

Electrostatic-induced Assembly of Graphene-encapsulated Carbon@Nickel-Aluminum Layered Double Hydroxide Core–Shell Spheres Hybrid Structure for High-energy and High-power-density Asymmetric Supercapacitor

Shuxing Wu, Kwan San Oscar Hui, Kwun Nam Hui, and Kwang Ho Kim

ACS Appl. Mater. Interfaces, **Just Accepted Manuscript** • DOI: 10.1021/acsami.6b09355 • Publication Date (Web): 12 Dec 2016

Electrostatic-induced Assembly of Graphene-encapsulated Carbon@Nickel-Aluminum Layered Double Hydroxide Core–Shell Spheres Hybrid Structure for High-energy and High-power-density Asymmetric Supercapacitor

Shuxing Wu,[†] Kwan San Hui,*[,‡] Kwun Nam Hui,*[,§] and Kwang Ho Kim*[,†,∥]

[†]Department of Materials Science and Engineering, Pusan National University, San 30 Jangjeon-dong, Geumjeong-gu, Busan 609-735, Republic of Korea.

[‡]School of Mathematics, University of East Anglia, Norwich, NR4 7TJ, United Kingdom

[§]Institute of Applied Physics and Materials Engineering, University of Macau, Avenida da Universidade, Macau, China

[∥]Global Frontier R&D Center for Hybrid Interface Materials, Pusan National University, 30 Jangjeon-dong, Geumjung-gu, Busan 609-735, South Korea

*Corresponding author:

E-mail: k.hui@uea.ac.uk (Kwan San Hui)

Tel: +44 (0) 1603 59 2582

E-mail: bizhui@umac.mo (Kwun Nam Hui)

Tel: +853 8822-4426; Fax: +853 8822-2426

E-mail: kwhokim@pusan.ac.kr (Kwang Ho Kim)

Tel.: +82 51 510 3391; Fax: +82 5 1514 4

ABSTRACT

Achieving high energy density while retaining high power density is difficult in electrical double-layer capacitors and in pseudocapacitors considering the origin of different charge storage mechanisms. Rational structural design became an appealing strategy in circumventing these trade-offs between energy and power densities. A hybrid structure consists of chemically converted graphene-encapsulated carbon@nickel-aluminum layered double hydroxide core–shell spheres as spacers among graphene layers (G-CLS) used as an advanced electrode to achieve high energy density while retaining high power density for high-performance supercapacitors. The merits of the proposed architecture are as follows: (1) CLS act as spacers to avoid the close restacking of graphene; (2) highly conductive carbon sphere and graphene preserve the mechanical integrity and improve the electrical conductivity of LDHs hybrid. Thus, the proposed hybrid structure can simultaneously achieve high electrical double-layer capacitance and pseudocapacitance resulting in the overall highly active electrode. The G-CLS electrode exhibited high specific capacitance (1710.5 F g^{-1} at 1 A g^{-1}) under three-electrode tests. An ASC fabricated using the G-CLS as positive electrode and reduced graphite oxide as negative electrode demonstrated remarkable electrochemical performance. The ASC device operated at 1.4 V, and delivered a high energy density of 35.5 Wh kg^{-1} at a 670.7 W kg^{-1} power density at 1 A g^{-1} with an excellent rate capability, as well as a robust long-term cycling stability of up to 10 000 cycles.

KEYWORDS: Asymmetric Supercapacitor, Graphene, Carbon sphere, Nickel-Aluminum Layered Double Hydroxide, Electrostatic Assembly.

INTRODUCTION

Supercapacitors (SCs), that includes electric double-layer capacitors (EDLCs, generally composed of carbonaceous materials) based on electrostatic adsorption/desorption, and pseudocapacitors (such as in transition metal oxides/hydroxides) based on Faradaic reactions, are advantageous for their high power density, fast charge propagation dynamics, and long cycle life compared with batteries.[1-2] However, the main obstacle impeding the development of high-performance SCs is the trade-off between high energy and high power densities. Such that, achieving a high energy density while retaining high power density is difficult to realize in electrical double-layer capacitors and pseudocapacitors considering the origin of different charge storage mechanisms. Generally, the energy density of a SC is a function of the capacitance and the working potential window.[3] Even with the exploration and development of new electrode materials that possess high capacitance, obtaining electrode materials with simultaneous high energy and power densities remains challenging. Alternatively, the high energy density of electrode can be achieved by maximizing the operation cell voltage. For instance, ionic liquids or organic electrolytes have been used as electrolytes because of their immense working potential window (> 2V).[2] Unfortunately, these electrolytes are usually more expensive than aqueous electrolytes, which hinders it from penetrating the general energy storage market.

The integration of a battery-type Faradaic electrode (cathode) and a capacitor-type electrode (anode) to assemble an asymmetric supercapacitor (ASC) has been recently found to be an effective approach in increasing cell voltage in aqueous electrolytes.[3] With this configuration, ASC possesses the advantages of different potential windows of the

two electrodes to broaden the cell voltage (up to 2 V), which enhance energy density.[3-4] Although extensive studies on SCs aim to boost their energy density while retaining high power density, much attention has also been paid to the development of low-cost environmentally friendly materials with long cycle life. Electrochemically active layered double hydroxides (LDHs) have long been considered promising electrode materials for SCs because of their intriguing features that include composition versatility, great theoretical capacitance values, low cost, and environmental benignity.[5-7] LDHs are an important class of synthetic two-dimensional (2D) layered materials consisting of $M^{II}(OH)_2$ stacked layers, where a number of metal M^{II} cations are isomorphously replaced by metal M^{III} cations that neutralize positively charged host layers with A^{n-} anions.[8-11] The most studied LDHs can be represented by the general formula $[M^{II}_{1-x} M^{III}_x(OH)_2]^{x+}(A^{n-})_{x/n} \bullet mH_2O$, where M^{II} (e.g., Mn, Fe, Ni, Cu, Zn) and M^{III} (e.g., Cr, Fe, Co, Al, Ga) are di- and trivalent metal cations, respectively, and A^{n-} (e.g., CO_3^{2-}, NO_3^-) is an anion.[8-10] However, the obtained LDHs capacitance in experiments is usually far below its theoretical capacitance given its high electrical resistance.

To overcome this issue, carbonaceous materials, such as carbon nanoparticles [12], carbon nanofibers,[13] carbon nanotubes,[14] graphene,[15-16] and conductive polymers[17] have been widely used as matrices to improve the electrical conductivity of LDHs. Graphene, a 2D monolayer of carbon atoms packed into honeycomb lattice, is particularly emerging as one of the most appealing matrices because of its larruping properties such as superior electrical conductivity (10^6 S cm^{-1}) and high theoretical specific surface area (2630 m^2 g^{-1}).[18-19] Furthermore, it can conduct paths to improve charge transfer and mass transport during the charging/discharging processes.[18] In this regard, LDHs/graphene hybrids or

composites, wherein LDHs are distributed onto the graphene surface or embedded into the graphene layers, have been prepared to achieve the full potential of the two complementing counterparts.[20-21] However, LDH materials are still prone to heavy aggregation during the electrochemical charge storage process because of the nonintimate connection between graphene layers and LHDs, which significantly increases contact resistance, and thus decreases specific capacitance.[22-24] Furthermore, a large volume expansion during the prolonged charge–discharge process is an intrinsic material problem, such that electrodes cannot maintain their integrity during the cycle processes resulting in poor cycling performance.[25] Therefore, the rational design of electrode architecture may contribute in alleviating the intrinsic materials degradation process and in simultaneously achieving high energy and power densities.

In this study, chemically converted graphene-encapsulated carbon@nickel-aluminum layered double hydroxide core–shell spheres (G-CLS) were fabricated in an aqueous environment through self-assembly between negatively chemically converted graphene (CCG) colloid and positively charged carbon@nickel-aluminum layered double hydroxide core–shell spheres (CLS). CCG colloid was obtained through the chemical reduction of graphene oxide prepared by modified Hummers method. CLS was synthesized via the co-assembly of NiAl LDH nanosheets on carbon spheres (CSs), and was functionalized with cetyltrimethylammonium bromide (CTAB) afterwards. The electrostatic attractive interactions of the two species formed G-CLS, whose main features are shown in Scheme 1. The unique design and fabrication of the hybrid structure include the following advantages: (I) the vertically grown NiAl LDH nanosheets surfaces on the CSs prevent NiAl LDHs aggregation and accommodate

volume change during the charging-discharging process;[9, 26] (II) the incorporated CLS can serve as spacers to mitigate the restacking of individual graphene effectively; (III) the mutual electrostatic interactions of CCG and CLS enable the direct interfacial contact between them, which remarkably shortens the diffusion path; (IV) the graphene can be utilized as electron mediators for shuttling electrons, and thus, a high electrical conductivity can be maintained for the overall electrode. Owing to this unique structural architecture, the G-CLS electrode exhibits a remarkably high specific capacitance of 1710.5 F g^{-1} at 1 A g^{-1}. The ASC device, composed of G-CLS//G operated at 1.4 V, delivered a high energy density of 35.5 Wh kg^{-1} at a 670.7 W kg^{-1} power density with an excellent rate capability (an energy density of 32.1 Wh kg^{-1} at power density of 5578.1 W kg^{-1}) and a robust long-term cycling stability of up to 10 000 cycles.

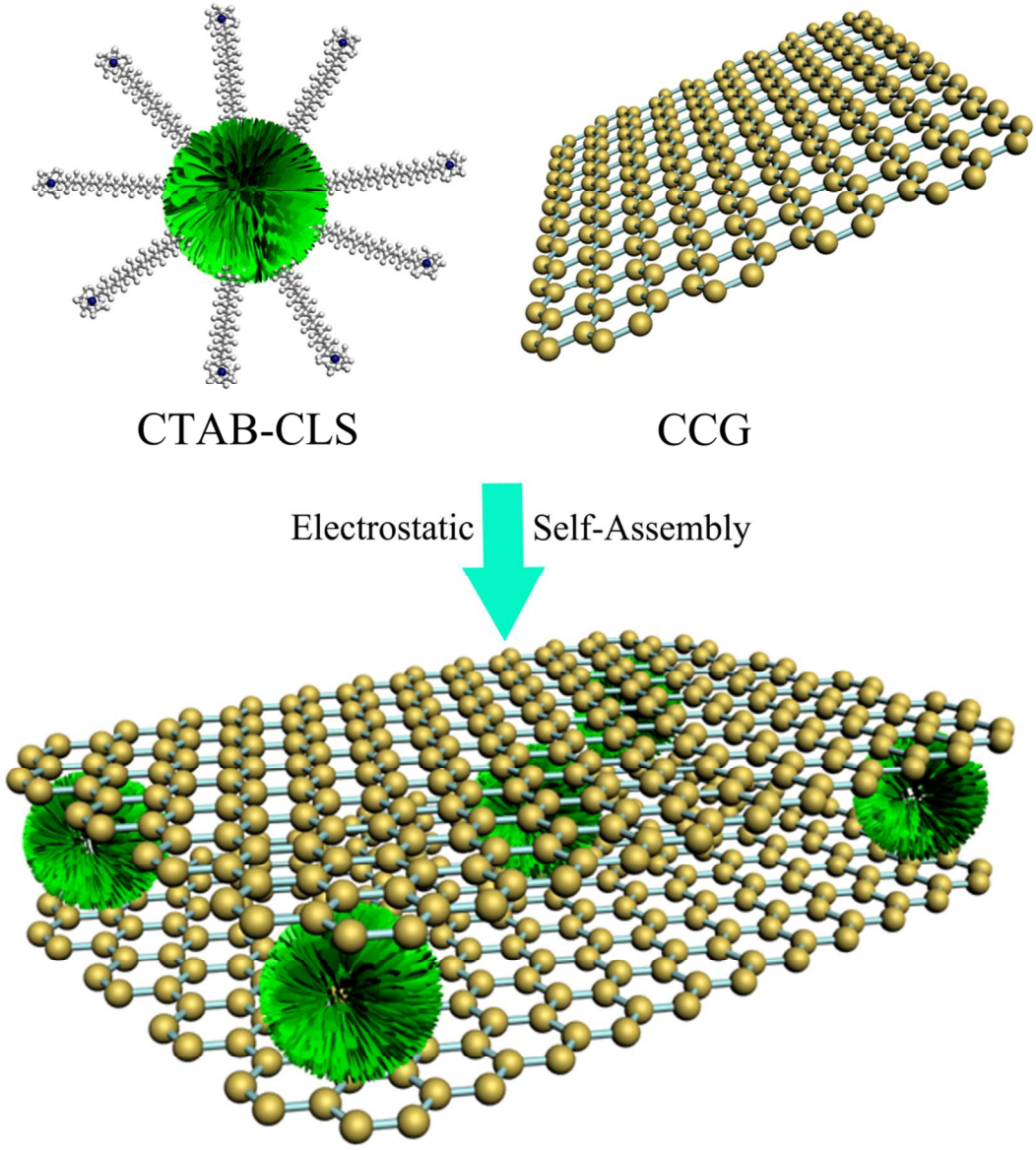

Scheme 1. Schematic diagram of the G-CLS hybrid structure.

EXPERIMENTAL SECTION

Synthesis of CCG colloid. Graphite oxide was prepared using natural graphite (Asbury Carbons) through the modified Hummers method as reported elsewhere [27-28] . Similar to a typical experiment, graphite flakes (3.0 g) were stirred in concentrated sulfuric acid (70

mL) at room temperature (RT), followed by the addition of sodium nitrate (1.5 g). Potassium permanganate (9.0 g) was added slowly to keep the solution temperature lower than 20 °C while maintaining the reaction flask in an ice bath. The entire reaction system was subsequently placed into a 35 °C water bath for 30 min, which formed slurry. Afterwards, 140 mL deionized (DI) water was added, and the suspension was stirred for another 15 min. The solution was diluted with additional DI water (500 mL) and treated with 20 mL of H_2O_2 (30 wt %) until no gas was produced, which changes the solution color from brown into yellow. The mixture was filtered and washed with 1:10 HCl aqueous solution (250 mL) to provide the graphene oxide solution. To verify the absence of Cl^- ions in the as-obtained graphene oxide solution, the supernatant was tested with $AgNO_3$ solution to confirm that no precipitation was formed. The obtained graphene oxide solution was freeze-dried to obtain brownish graphite oxide power. Graphite oxide was exfoliated through sonication in 0.25 mg mL^{-1} graphite oxide aqueous solutions for 60 min, and then, centrifugation at 3000 rpm for 30 min. CCG colloid was prepared via chemical reduction [29]. The as-obtained GO solution was adjusted to pH 10–10.5 by ammonia solution (28 wt % in water), in which the hydrazine solution (35 wt % in water) was added under vigorous stirring after. The mixture was placed in a water bath (95 °C) for 60 min without stirring to produce jet-black colloid.

Synthesis of CLS. CSs were prepared by a classical hydrothermal carbonization procedure.[30] The glucose obtained from biomass was chosen as the carbon source. CLS was fabricated using the facile solvothermal method.[31] In a typical synthesis, CSs were dispersed into absolute ethanol under ultrasonication for 30 min, and then, stirred vigorously for another 30 min. Successively, 0.009 mol of $Ni(NO_3)_2 \cdot 6H_2O$ and 0.003 mol

of $Al(NO_3)_3 \cdot 9H_2O$ were dissolved into 80 mL of CSs suspension (3 mg mL^{-1}) that contains 0.04 mol urea. The resulting suspension was transferred to a Teflon-lined autoclave vessel. The solvothermal reaction was performance at 140 °C for 14 h. After cooling down to RT, the composites were separated through centrifugation, washed with DI water and ethanol, and air-dried at 60 °C for 12 h. For comparative purposes, the hydrothermal method was adopted using DI water instead of absolute ethanol (denoted as CLH).

Synthesis of G-CLS. The CLS was functionalized using CTAB. CTAB was dissolved in 50 mL of DI water (0.5 wt %), and CLS powder was added after. The resulting dispersion was stirred for 5 h at RT. The functionalized CLS was collected by centrifugation, washing, and redispersion in DI water. Finally, the pH of the functionalized CLS dispersion (0.25 mg mL^{-1}) was adjusted to 9.5 using a diluted ammonia solution. The CCG self-assembly and functionalized CLS were accomplished through electrostatic interactions. Briefly, 50 mL of functionalized CLS dispersion was added into 50 mL of CCG colloid (0.25 mg mL^{-1} of GO) under mild stirring at RT. The final product (G-CLS) was obtained by centrifugation, followed by washing and air drying. The nominal mass ratio of CCG, NiAl LDHs, and CSs in G-CLS composite is 1:0.165:0.835.

Characterization. The powder X-ray diffraction (XRD) was recorded with a Rigaku MPA-2000 using filter Cu kα radiation (λ = 1.5418 Å) with a 40 kV accelerating voltage and a 40 mA current. The samples were scanned at 2θ, from 5° to 80°. Scanning electron microscopy (SEM) observations were performed using a Tescan MIRA3 LMH. The transmission electron microscopy (TEM) image, energy-dispersive spectrometry (EDS) mapping, and selected area electron diffraction (SAED) pattern were completed on a

Titan G2 60-300 FEI transmission electron microscope. Raman spectroscopy was conducted using a Jobin-Yvon Horiba HR800 UV Raman microscope. This instrument used a laser of 514 nm wavelength as its excitation light source. Specific surface area (SSA) and porosity of materials were examined by Brunauer-Emmett-Teller method (BET, Micromeritics 3Flex). The X-ray photoelectron spectroscopy (XPS) data were collected on a Thermo VG Escalab 250 X-ray photoelectron spectrometer. Binding energy (BE) was calibrated with C 1s = 284.6 eV.

Electrochemical Test. The electrochemical tests were conducted on an IVIUM Nstat electrochemical station. The working electrode was fabricated by mixing acetylene black and polytetrfluoroethylene (PTFE) with ethanol in a mass ratio of 85:10:5. The mixture was carefully placed onto nickel foam (1 cm × 1 cm), and then dried in a vacuum oven at 80 °C. The three-electrode tests were carried out with saturated calomel electrode (SCE, Hg/Hg_2Cl_2) as the reference electrode and platinum foil as the counter electrode. The electrolyte was a 6.0 M KOH aqueous solution. The specific capacitance of a single electrode was calculated from the charge/discharge curves according to the following equation:[32]

$$Cs = \frac{2i_m \int V dt}{V^2 \Big|_{Vi}^{Vf}} \qquad (1)$$

where $i_m = I/m$ (A g^{-1}) is the current density, I is the discuss current, m is the mass of active material in the electrode, V (V) is the potential window with initial and final values of V_i and V_f, respectively.

The ASCs were assembled with G-CLS as the positive electrode and reduced graphite oxide (rGO)[33] prepared through the pyrolysis of graphite oxide as the negative electrode. The rGO to G-CLS mass ratio is around 5.7 according to the equation:

$$\frac{m_+}{m_-} = \frac{C_- \Delta V_-}{C_+ \Delta V_+} \quad (2)$$

The energy (E, Wh kg^{-1}) and power (P, W kg^{-1}) densities of ASCs were calculated as follows:

$$C = \frac{I \times \Delta t}{M} \quad (3)$$

$$E = \frac{(\int_{t_0}^{t} \Delta V \, dt \cdot I)}{M} \quad (4)$$

$$P = \frac{E}{t - t_0} \quad (5)$$

where M (g) is the total mass of the positive and negative electrodes ($M = m_+ + m_-$), ΔV (V) is the voltage scan range, I (mA) is the constant discharge, t (s) is the discharge starting time, t_0 (s) is the end time of discharge, Δt is the discharge time, and C (mAh g^{-1}) is the specific capacitance of ASCs.

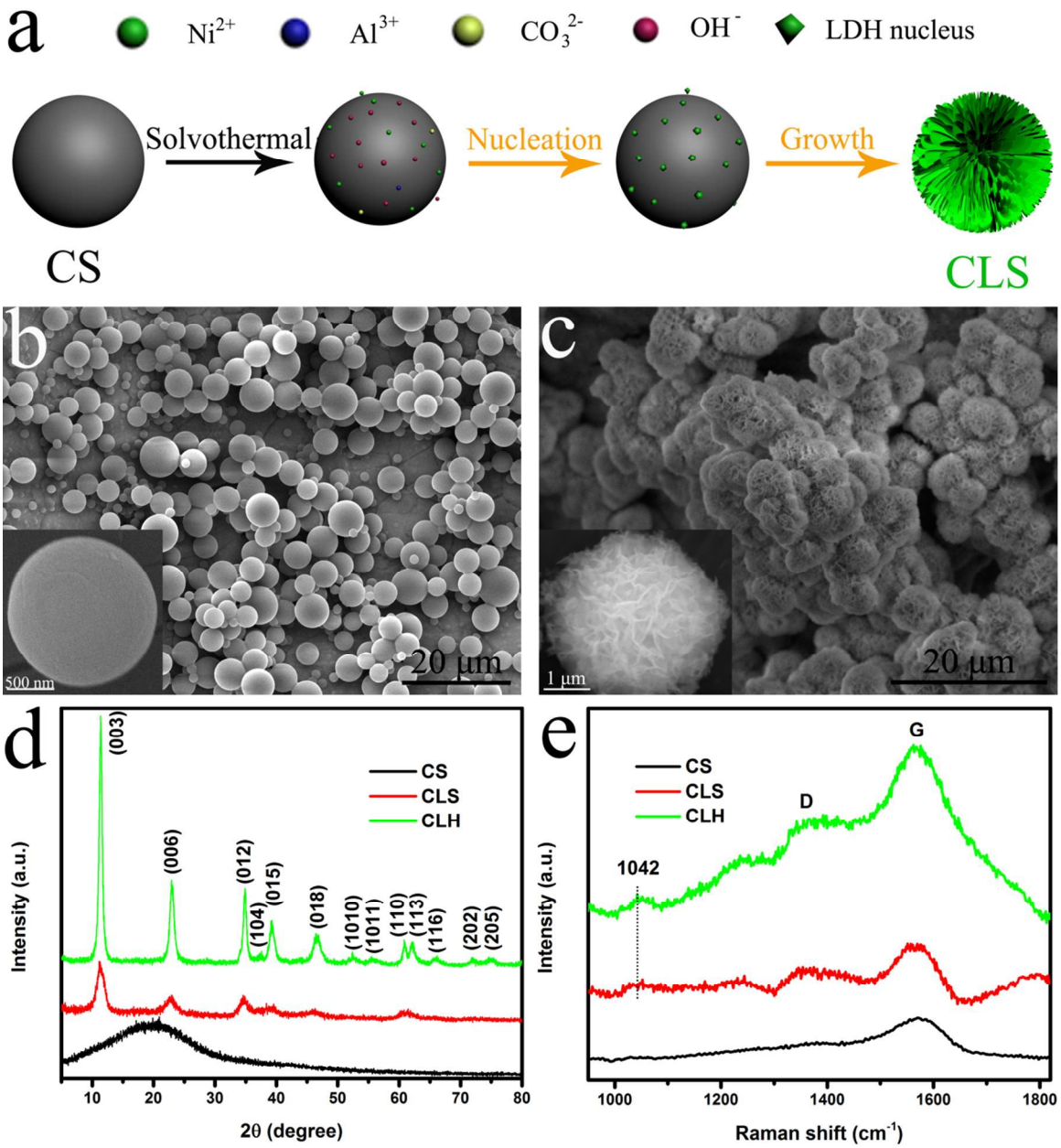

Figure 1. (a) Schematic illustration of the proposed CLS evolution process. (b) SEM images of CSs. (c) SEM images of CLS. (d) XRD patterns and (e) Raman spectrum of the CS, CLH, and CLS.

RESULTS AND DISCUSSION

The CLS fabrication process is displayed in Figure 1a. The growth of NiAl LDHs nanosheets on CSs underwent the following reactions: (i) Ethanol and NO_3^- experienced a redox reaction producing hydroxyl ions at 140 °C: $4CH_3CH_2OH + NO_3^- \rightarrow CH_3CHO + NH_3 + OH^- + 2H_2O$;[34] (ii) The urea decomposition controlled the carbonate supply: $CO(NH_2)_2 + 2H_2O \rightarrow H_2CO_3 + NH_3$;[35] (iii) Ni^{2+}, and Al^{3+} ions reacted with OH^- to generate aluminum aquohydroxo complexes and nickel hydroxides;[36] (iv) The nickel/aluminum salts were converted to NiAl LDHs nanosheets by olation reactions and crystallization;[37] (v) The LDH phase crystallization eventually bonded with the CSs. Nucleation and growth, Ostwald ripening and self-assembling contributed to the hierarchical core–shell architecture of CLS.[38] Figure 1b shows the SEM images of CSs obtained using the hydrothermal method from glucose at 180 °C. The SEM images indicated the solid spheres with smooth surfaces of the obtained CSs in addition to their good monodispersity, which ranged from 1 μm to 6 μm. According to the previous report, these CSs were mainly polysaccharides containing abundant −OH and C═O groups on the surface,[39] which facilitate the Ni/Al precursor nucleation during the LDH growth. As expected, NiAl LDH nanosheets were uniformly anchored on the surface of each CS to form a core–shell sphere (i.e., CLS) through the solvothermal process (Figure 1c). The LDH material was fabricated with similar processes except for the replacement of absolute ethanol with DI water through hydrothermal method (CLH) for comparative purposes. Results show that CLH consisted of a large number of LDH flakes self-assembled to form flower-like sphere, where no core–shell architecture was observed (Figure S1). In contrast, the CLS exhibited a mesoporous sphere morphology, where

LDH nanosheets coated the CSs surfaces to provide an open and close-grained structure. The LDH shell is specifically mainly composed of thin interconnected nanosheets because the use of ethanol altered the surface energy and diminished the crystal growth rate.[40] Thus, the CLS is highly accessible to electrolytes for energy storage considering the intriguing mesoporous sphere architecture. Figure 1d provides information on the crystallinity of the products. The CS diffraction pattern depicted a reflection characteristic of amorphous carbon.[41] After the LDH coating, the reflections indexed to a typical rhombohedral phase NiAl hydrotalcite in R-3m (166) space group (JCPDS No. 15-0087) were observed. A series of (00*l*) reflections in the XRD patterns at low 2θ values confirmed the characteristic of a layered structure. No CSs diffraction peaks were observed, proving that CSs are homogeneously surrounded by LDHs. No excrescent peaks from other crystallized phased were detected as well, implying the formation of the pure LDH structure. The CLS sample showed relative broad XRD patterns compared with that of CLH samples, indicating that the LDH crystals of CLS sample possesses smaller sizes consistent with the SEM images results. However, the XRD patterns of CLS exhibited poor crystallinity compared with that of CLH. This poor crystallization of CLS implies more ions transportation channels within the mesoporous structure, which favored the achievement of fast ion diffusion kinetics.[42] Furthermore, the XRD data showed that the basal spacing of the CLS pattern (8.0 Å) is larger than that of CLH (7.8 Å), which can facilitate the OH^- ions diffusion and enhance high rate capability. A larger basal spacing also implies a higher intercalated H_2O and CO_3^{2-} contents that can increase the hydrophilicity of CLS and render close contact between CLS with electrolyte, and thus, improve electrochemical performance. Nevertheless, the presence of CSs can be

confirmed through Raman spectroscopy. Figure 1e shows the Raman spectra of CSs, CLH, and CLS. Two major bands corresponding to the D-band (1350 cm^{-1}) and G-band (1570 cm^{-1}) of carbon were found across all spectra. In addition, the CLS and CLH spectra showed a peak centered at 1042 cm^{-1}, corresponding to the Raman peak of NiAl LDH.[15]

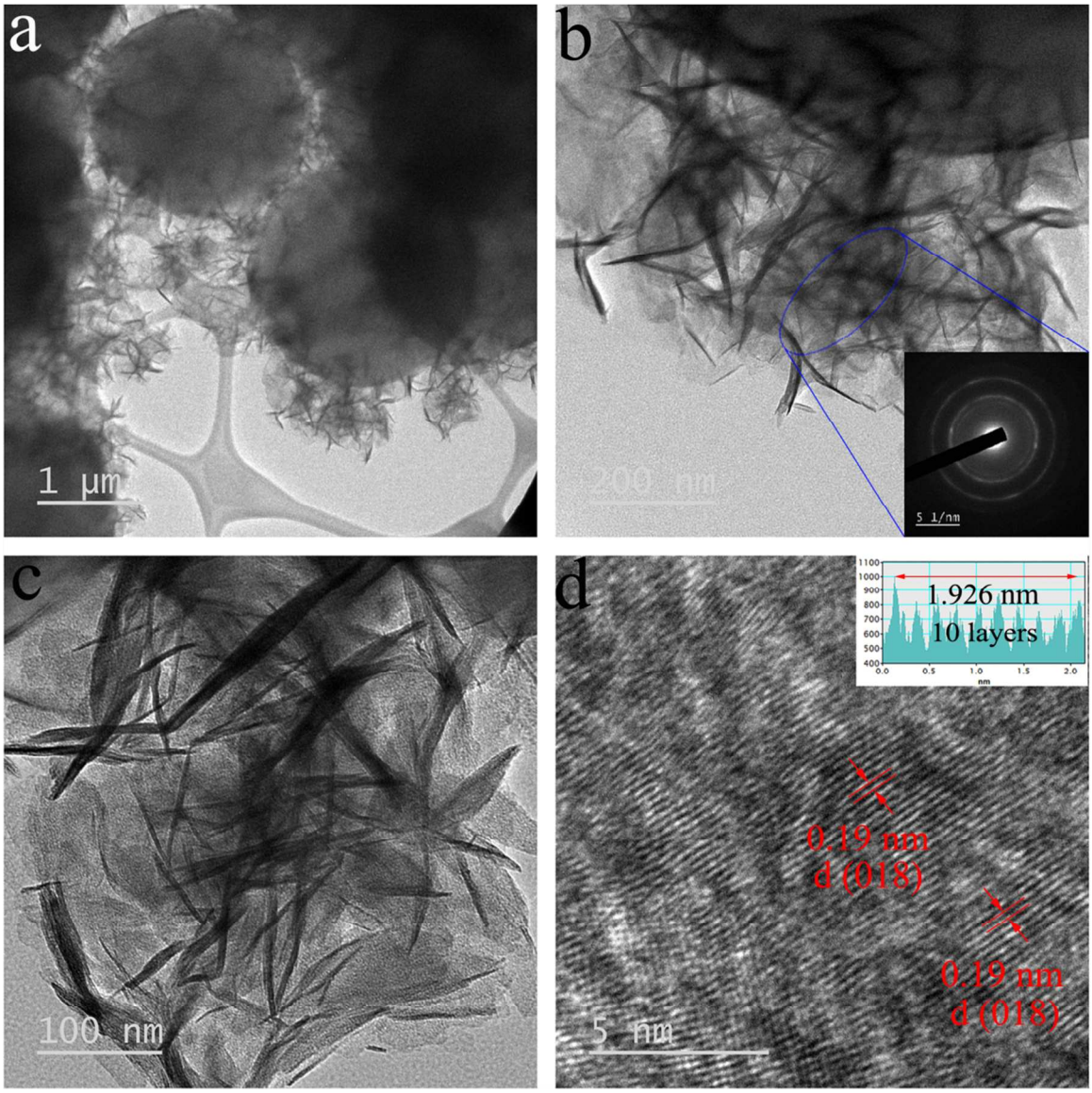

Figure 2. TEM (a, b, c, and d) and SAED (inset in b) pattern images of the CLS.

The TEM image of CLS (Figure 2a, b) clearly shows a representative core–shell structure, from which a distinctive CS core and a NiAl LDH nanosheets shell are evident. The NiAl LDHs are highly dispersed and firmly grafted on the CSs. This heterostructure provides the facile penetration of electrolyte, and also buffers the volume changes during the charging-discharging process. Further analysis of the selected area electron diffraction (SAED) pattern revealed the polycrystalline nature of NiAl LDHs nanosheets (inset in Figure 2b), which agreed well with XRD data. The amplified TEM image in Figure 2c revealed NiAl LDH nanosheets exhibiting foldaway silk-like morphology that is beneficial for shorting ion diffusion paths because of its large aspect ratio and its ability to facilitate the surface-dependent electrochemical reaction process.[43-44] High-resolution TEM image (Figure 2d) shows the visible lattice fringes with an equal inter-planar distance of 0.19 nm that corresponding to the (018) plane of LDHs.

To obtain detailed information about the surface electronic states of the as-prepared CLS hybrid, XPS measurement was performed. The C 1s, O 1s, Ni 2p, and Al 2p peaks (as shown in Figure S2) were evidently predominant in the CLS composite. The high-resolution spectrum of C 1s in Figure S3a can be deconvoluted into four peaks: C═C (284.5 eV), C-O (285.1eV), C═O (285.9 eV), and O-C═O (288.3 eV).[45] The relatively high intensity of O-C═O (CO_3^{2-}) indicates that CO_3^{2-} anion is a NiAl LDH component, consistent with the XRD result. The O 1s spectrum (Figure S3b) with a strong peak at 531.5 eV is associated with bound hydroxide groups (OH^-).[46] Two major peaks with binding energies at 856.2 and 873.8 eV corresponding to Ni $2p_{3/2}$ and Ni $2p_{1/2}$, respectively, yielded a spin-energy separation of 17.6 eV, which correlated with previously reported data.[7] Furthermore, their associated satellite peaks (indicated as “Sat”)

located at 863.3 and 880.1 eV were also observed. Figure S3d shows the peak centered at 73.4 eV, relating to the Al 2p, as well as the Al^{3+} levels.[26]

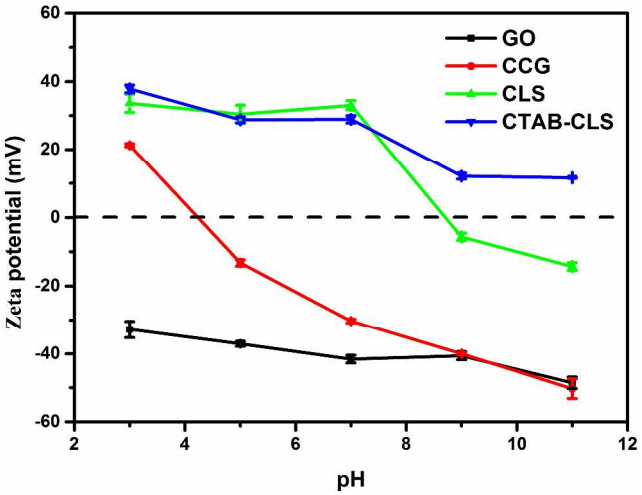

Figure 3. Zeta potential profiles of GO, CCG, and CLS before and after functionalization with CTAB.

The rational synthesis and self-assembly of G-CLS were developed via electrostatic interactions. Figure 3 shows the zeta potentials of GO, CCG, and CLS before and after CTAB functionalization in DI water as a function of pH. Comparison of the profiles of CLS before and after functionalization shows that CLS exhibited a negative Zeta potential at pH higher than 9 before functionalization, whereas a positive Zeta potential was observed with CTAB after functionalization. Such change of surface charge was obtained by grafting to a cationic surfactant (CTAB) on the CLS surface.[47] Furthermore, the GO dispersed in water constantly displayed negative potentials due to the ionization of carboxylic acid ($COOH^-$), epoxy (COC^-), and hydroxyl (OH^-) on the GO sheets as the pH value varied from 3 to 11.[29, 48-49] Moreover, the Zeta potential of the CCG dispersion remained positive before reaching an isoelectric point at pH 4–5. The negative Zeta

potential in the pH range 5−11 is attributed to the incomplete reduction of their partial oxygen functional groups. Within the paradigm of colloidal chemistry, the final CCG deposition morphologies greatly depended on the pH of colloidal dispersions.[50] At high pH, single-layer identity can be preserved because of the electrostatic repulsion emanating from the negatively charged functional groups. With this concept in mind, the CLS after functionalization was mixed with CCG dispersion (DI water, pH 9.5) as demonstrated in Figure 4.

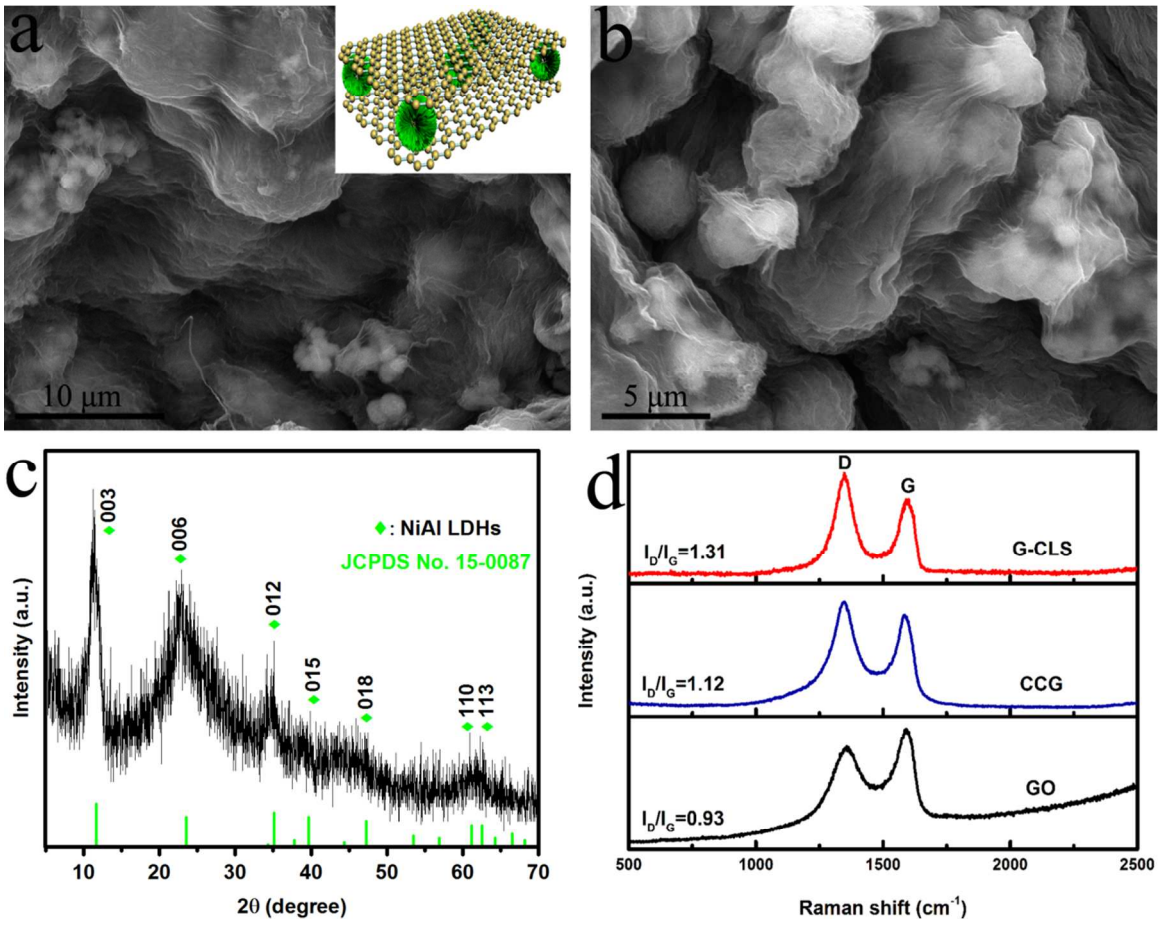

Figure 4. (a, b) SEM images of G-CLS. (c) XRD pattern of the G-CLS and standard X-ray diffraction pattern. (d) Raman spectra of GO, CCG, and G-CLS.

The hierarchical hybrid structure comprising CLS and CCG was investigated by SEM. Figures 4a and b illustrate the rough and crinkled terrains of the CCG nanosheets encapsulated CLS attributing to the flexible and thin 2D graphene sheets.[24] Note that CLS served as spacers to intercalate into the CCG nanosheets, which allow CCG sheets to develop a series of vertices, winkles, and ripples that can effectively prevent restacking. The strong electrostatic interaction between CLS and CCG sheets was clearly confirmed by the intimate coverage of CCG sheets on the CLS contour. Moreover, the continuous nature of CCG sheets in the lateral dimension help to facilitate the electron transport and to buffer the strain from the CLS volume change during the charging/discharging process.[24, 51] The resulting G-CLS composites were further characterized by XRD. Remarkably, all diffraction peaks were well indexed to the typical rhombohedral phase NiAl LDH (JCPDS No. 15-0087, Figure 4c). In addition, no conventional stacking peak (002) of graphene sheets was observed at 26.6°, which implies the homogeneous dispersion of graphene sheets on the CLS surface.[31] Furthermore, the disorder sp^2 characteristic of graphene was investigated by Raman spectroscopy. All three samples displayed two characteristic peaks at approximately 1350 and 1580 cm^{-1}, which should be ascribed to the well documented D and G bands, respectively. The D band is caused by defective or disordered bent sites, whereas the G band originated from phonon vibrations in sp^2 carbon materials.[52] Generally, the integrated intensity ratio of the D and G bands (I_D/I_G) is measured to qualitatively analyze the structural defects and disorder of carbon materials.[53] Compared with GO, the I_D/I_G ratios of graphene nanosheets obtained by the chemical reduction of GO and G-CLS hybrids increased from 0.93 to 1.12 and 1.31, respectively, which suggests increased structural defects on the G-CLS; this

increase is evidently related to the intimate contact between CLS species and graphene.[54] Figure S4 shows the N_2 adsorption-desorption isotherms of CLH, CLS, and G-CLS, and the Barrett-Joyner-Halenda (BJH) pore size distribution of G-CLS. All the N_2 adsorption-desorption isotherms exhibit a type-IV hysteresis loop at a relative pressure between 0.4 and 0.9.[55] Based on the BET method, the SSA of CLH, CLS and G-CLS are 21.12, 32.29 and 79.01 $m^2 g^{-1}$, respectively. The large SSA could enhance the capacitive performance by providing more active sites for redox reactions. Moreover, the mesoporous structure of G-CLS was confirmed by BJH pore size distribution (inset in Figure S4), with pores distribution mainly centered at about 3.75 nm. The pores will be easy to allow the electrolyte ions transport inside the G-CLS since the pore sizes of electrode material are larger than the size of the solvated ions. The high BET SSA and well-developed mesoporous structure of G-CLS is believed to be extremely beneficial for energy storage applications.

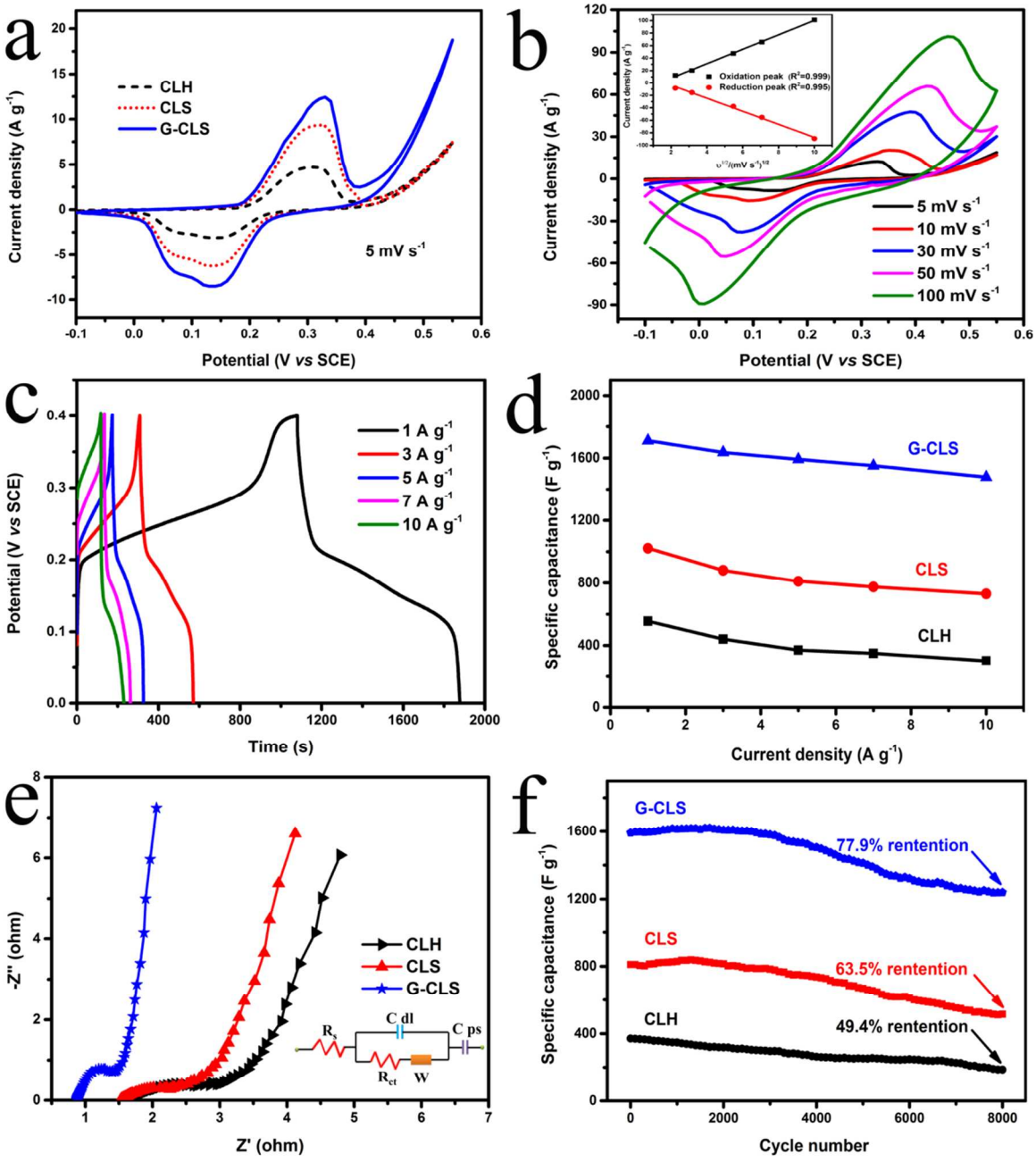

Figure 5. Electrochemical performance of the supercapacitor samples: (a) CV curves of the CLH, CLS and G-CLS at a scan rate of 5 mV S^{-1}. (b) CV curves of G-CLS at different scans. (c) Galvanostatic charge–discharge profiles of G-CLS with different current densities. (d) Specific capacitances of CLH, CLS, and G-CLS at different current densities. (e) Nyquist plots of CLH, CLS, and G-CLS. (f) Cycling stability performance of CLH, CLS, and G-CLS.

A series of CV measurements were performed with the potential window from −0.1 to 0.55 V relative to SCE. The CV curves of CLH, CLS, and G-CLS at a constant scan rate of 5 mV s^{-1} are shown in Figure 5a. A distinct pair of redox peaks can be clearly seen in the CV curves. These well-defined pair of redox peaks can be attributed to the reversible redox reaction of Ni^{2+}/Ni^{3+} in alkaline electrolyte:

$$Ni(OH)_2 + OH^- \leftrightarrow NiOOH + H_2O + e^- \quad (6)$$

This distinct redox feature presents that the capacitance originated primarily from the Faradaic pseudocapacitance. Given the same electrode preparation and testing conditions, the enclosed area of G-CLS is larger than that of CLH and CLS, indicating the better capacitive behavior of this composite material. The rational G-CLS design includes the following merits to achieve superior electrochemical performance. First, the core–shell architecture of CLS consists of vertically grown LDH sheets on carbon spheres can offer great access of the electrolyte to the active surface of the LDH, resulting in superior Faradaic reaction. Second, a highly conductive CCG serves as a conducting pathway to facilitate the electron transport during the charge/discharge process and acts as an ion reservoir to sustain high rate capability. Third, flexible CCG sheets can preserve the mechanical integrity of LDH electroactive materials during pro-long cycling leading to excellent cycling stability. The CV responses of the G-CLS electrode performed at different scan rates (5–100 mV s^{-1}) are presented in Figure 5b. The shape of the curves is well-retained up to the highest scan rate, which indicates the fast ionic diffusion of electrodes. Along with the increased scan rate, the current response increased accordingly, suggesting the good reversibility of the fast charge–discharge response of the materials. In addition, the anodic and cathodic peaks shifted to more positive and negative position,

respectively as the scan rate increased because of the rising internal diffusion resistance of the pseudoactive material.[56] The plot of the anodic and cathodic peak current densities against the square root of the scan rate (inset of figure5b) shows a linear correlation that reveals that the electrochemical process is diffusion-controlled process. Furthermore, the linear plot of the anodic peak current density is mirror-image symmetrical to the linear plot of the cathodic peak current density, which suggests the immense reversibility of the G-CLS electrode. The results clearly demonstrate that the G-CLS capacitance is attributed from the double layer and diffusion-controlled redox processes.[57-58] A closer analysis of the voltammetric scan rate dependence renders one to distinguish quantitatively the contribution fraction of the capacitance values. The capacitive values can be characterized by assessing the cyclic voltammetry data at different scan rates according to:[59]

$$Q = Q_{v=\infty} + \text{constant}\ (v^{-1/2}) \quad (7)$$

or

$$Q^{-1} = Q_{v=0}{}^{-1} + \text{constant}\ (v^{1/2}) \quad (8)$$

where $Q_{v=\infty}$ corresponds to the double layer charge (Coulomb), which is the value at $v = \infty$. $Q_{v=0}$ denotes the total charge, which is the value at $v = \infty$. Figure S5 plots the scan rate dependence of the charge. The calculations indicate that the contribution from diffusion-controlled redox capacitance is about 76.6%.

A series of GCD measurements were carried out at various current densities to quantify the capacitance and the rate capability of the electrode. Figure 5c shows the charge–discharge curves of the G-CLS under various current densities. The nonlinear charge–discharge curves demonstrate the pseudocapacitance nature, in line with the CVs. In

addition, a slightly symmetric shape during the charge–discharge process was observed, which implies a high Coulombic efficiency. Each discharge curve in Figure 5c exhibited two clear voltage stages: a fast potential drop (0.4−0.2 V) and a slow potential decay (0.2–0.1 V). The former arises from internal resistance, whereas the later signifies the pseudocapacitive feature of the electrode. According to equation (1), the G-CLS shows a specific capacitance as high as 1710.5 F g^{-1} (based on the whole sample mass) at a current density of 1 A g^{-1}, which is 1.7 and 3.1 times higher than that of CLS (1022.1 F g^{-1}) and CLH (555.1 F g^{-1}). Remarkably, the proposed G-CLS electrode showed superior performance compared to most other state-of-the-art nanostructured supercapacitors based on LDH and graphene (Table S1). Rate capability is an important factor in evaluating the performance of supercapacitors for high rate applications. The specific capacitances of the three samples at different charge–discharge current densities are shown in Figure 5d. Within the entire current density range, the G-CLS exhibited substantially higher specific capacitance compared to the other two samples (Figure S6), which is consistent with the CV results. At the current density of 10 A g^{-1}, 86.4% of the capacitance (from 1710.5 F g^{-1} to 1477.6 F g^{-1}) was retained for the G-CLS, superior to CLS and CLH.

AC electrochemical impedance spectroscopy (EIS) is a well-developed technique used to explore the parameters affecting the performance of electrodes, including their conductivity, charge transfer behavior, and diffusion property. Figure 5e displays the Nyquist plots of the G-CLS, CLS, and CLH electrode, representing the characteristic quasi-semicircle in the high- and medium-frequency regions, as well as the linear component in the low frequency region. At very high frequencies, the intercept at real

part (Z') is the equivalent series resistance (R_s), which is a combinational resistance of the intrinsic resistance of the electrode, the bulk electrolyte and the resistance at the electrolyte/electrode interface. According to the equivalent circuit, the R_s for G-CLS is 0.86 Ω, which is lower than that of the CLS (1.53 Ω) and CLH (1.69 Ω). The semicircle in the high frequency region is ascribed to the charge transfer resistance (R_{ct}) caused by the Faradaic reaction and the double layer capacitance (C_{dl}) on the electrode surface.[60] A smaller semicircle diameter suggests that the R_{ct} for G-CSL is smaller because of the larger electroactive surface area of the material.[60] The straight line with an angle at almost 45° with the real part Z' corresponds to the Warburg resistance (Z_w) and is the result of the frequency dependence of ion diffusion in the electrolyte [61]. The corresponding equivalent circuits for the measured impedance spectra are shown in the Figure 5e inset. The impedance parameter values calculated from the complex nonlinear least-squares (CNLS) fitting are presented in Table S2. The cycling performances of the three electrodes were evaluated using a galvanostatic charge–discharge technique at 5 A g^{-1} (Figure 5f). Compared with the CLH (49.4%) and CLS (63.5%), the G-CLS samples exhibited enhanced charge–discharge stability (77.9%).

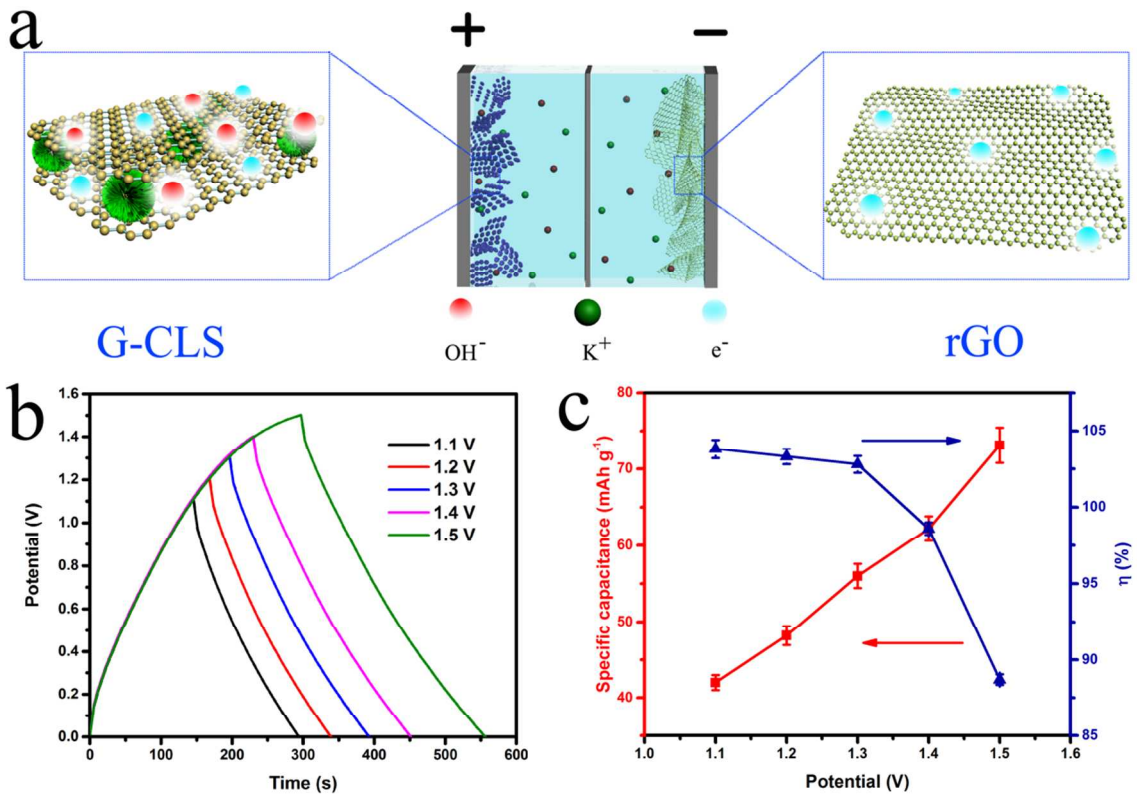

Figure 6. (a) Schematic illustration of ASC cell containing G-CLS and rGO as the positive and negative electrodes, respectively. (b) Galvanostatic charge–discharge of G-CLS//rGO with the increase of potential window. (c) Coulombic efficiency and specific capacitance of G-CLS//rGO in 6 M KOH electrolyte versus different cell voltages.

An asymmetric supercapacitor was fabricated using G-CLS and rGO as positive and negative electrodes, respectively, with a piece of polypropylene paper as separator in a 6 M KOH solution to access the G-CLS electrode for practical supercapacitor application. Prior to producing full cell devices, the mass loading of the two electrode materials was balanced, and the optimal mass ratio between two electrodes was calculated as 5.7:1 according to their individual electrochemical performances. Figure 6a displays the assembled structure for such ASC. The electrochemical behavior of the full cell device was studied thoroughly. The symmetrical charge–discharge curves indicated that the

device shows ideal capacitive behavior in the entire range of operation voltage from 1.1 to 1.5 V (Figure 6b). In addition, no obvious IR drop was observed, which can be attributed to the high conductivity of the electrodes. In order to determine the optimal cell voltage, the Coulombic efficiency (η) was calculated according to the following equation:

$$\eta = \frac{q_d}{q_c} \times 100\% \quad (9)$$

where q_d and q_c represent the total amounts of discharge and charge capacities of the cell, respectively. Figure 6c shows the Coulombic efficiency and the average specific capacitance versus cell voltage. The specific capacitance increases with the cell voltage, and the Coulombic efficiency decreases significantly when cycled above 1.4 V. This behavior may be attributed to a redox reaction, such as the evolution of H_2.[62] Thus, the cell voltage was fixed at 1.4 V in the subsequent research.

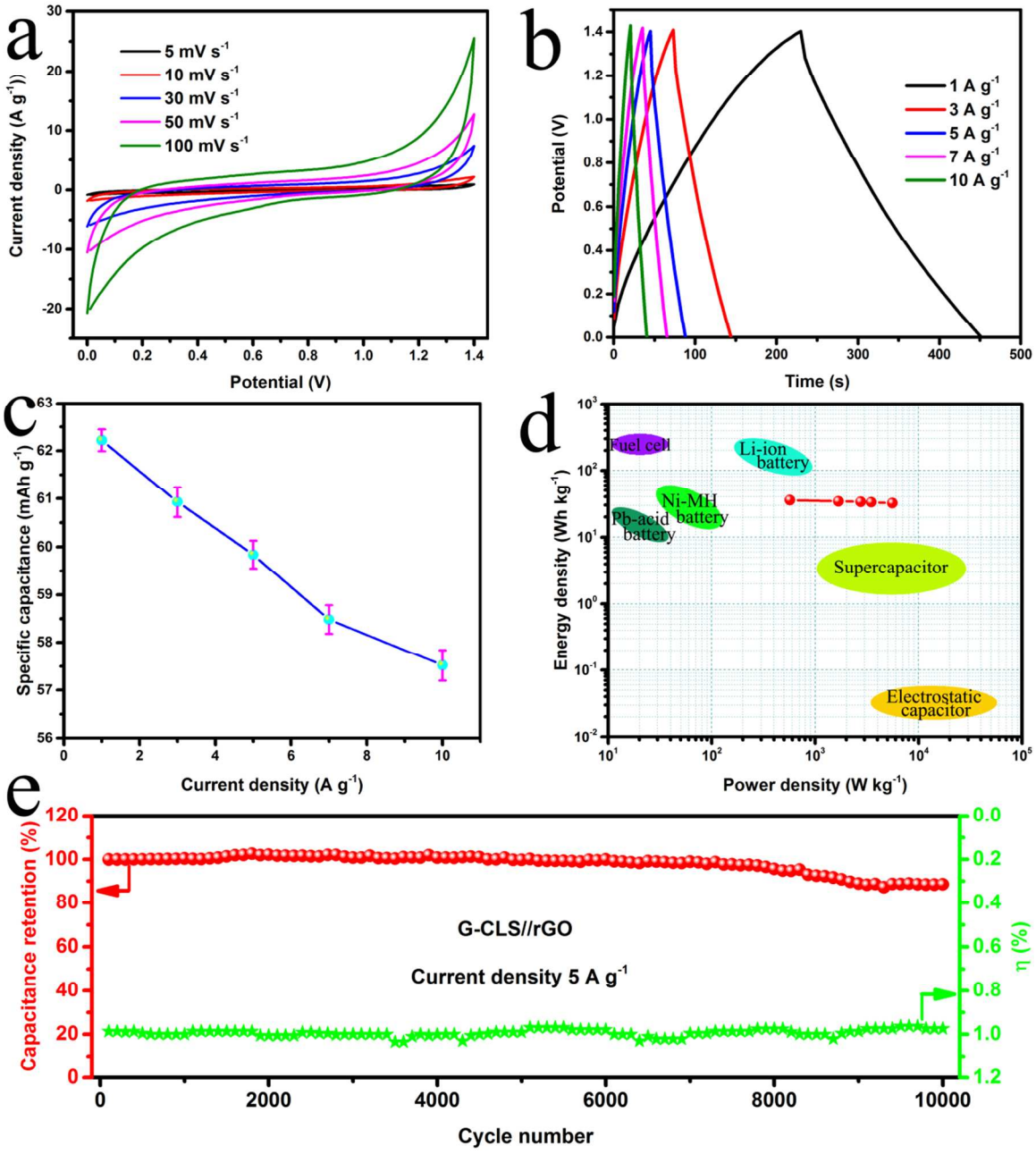

Figure 7. Electrochemical performance of the G-CLS//rGO. (a) CV curves. (b) Galvanostatic charge–discharge curves. (c) Specific capacitances at different current densities. (d) Ragone plot. (e) Cycling performance and Coulombic efficiency.

Figure 7a shows the CV curves for the G-CLS//rGO ASC device at various scan rates (ranging from 5 to 100 mV s^{-1}) within the potential range of 0−1.4 V. A rectangle-like shape was clearly observed across all scan rates. Even at high scan rate of 100 mV s^{-1}, the shape of the CV curves was retained, which demonstrates the desirable fast charge–discharge property for power devices. The GCD plots at different current densities (1–10 A g^{-1}) are shown in Figure 7b. The specific capacitance of the ASC was calculated based on the total mass of the electrodes (both positive and negative electrodes). The gravimetric specific capacitance as a function of the applied current density is plotted in Figure 7c. The specific capacitance values are 62.2, 60.9, 59.8, 58.5, and 57.5 mAh g^{-1} at current densities of 1, 3, 5, 7, and 10 A g^{-1}, respectively, revealing an excellent rate performance (92.4%).

A Ragone plot (Figure 7d), a behavior indicator for energy storage devices, was utilized to evaluate the performance of ASC in this study. Encouragingly, the energy density of the aqueous G-CLS//rGO ASC reached 35.5 Wh kg^{-1} at a power density of 670.7 W kg^{-1}, and even remained at 32.1 Wh kg^{-1} at a power density of 5578.1 W kg^{-1}, proving this rational G-GLS architecture could be an effective approach in achieving high energy density while retaining power density. Cycling stability is another critical parameter in determining the energy storage device for practical applications, and the long-life stability of our ASC was evaluated and shown in Figure 7e. The figure clearly shows that the designed G-CLS//rGO ASC device displays a remarkable cycling stability at 88.5% of the initial capacitance after 10 000 consecutive charge–discharge measurements. Remarkably, the Coulombic efficiency remained at ~100% during the 10 000 charge-

discharge cycling test. The tandem devices can power a red light-emitting diode (LED, 1.9 V) after being charged at 5 A g^{-1} for 40s (Figure S7).

The superior electrochemical behavior of our asymmetric full cells can be attributed to the following factors: First, the energy density of an SC is proportional to the square of the operating voltage; thus, increasing the operation voltage of ASCs is a promising strategy to improve the energy density of a SC.[63] As shown above, the optimized mass balance allowed the devices to operate at 1.4 V potential window with stable electrochemical behavior. Second, graphene has high electrical conductivity, excellent mechanical properties, superior electrochemical stability, and large surface area. These advantages enable high charge propagation dynamics, fast electron transport, long cycling life, and low internal resistance of the electrodes, which consequently enhance electrochemical performance. Third, the vertical growth of LDH nanosheets on CSs cores significantly increases the contact area between the LDH nanosheets and the alkaline electrolyte, which benefits the migration of electrolyte ions to the LDH surface, thus ensuring rapid redox reactions. Furthermore, the unique core–shell spheres can effectively prevent graphene aggregation. Briefly, the synergistic contribution of electrical double-layer capacitance from graphene and pseudocapacitance from LDH lead to superior electrochemical performance. All of the above results verified that the G-CLS//rGO ASC can simultaneously achieve the high energy density of G-CLS as a battery-type Faradic electrode (as energy source) and the high power density of rGO as a capacitor-type electrode (as power source). Such G-CLS hybrid structure shows promise for practical energy storage applications owing to its low cost, low toxicity, eco-friendliness, safety, and convenient air package advantages.

Conclusion

A self-assembly route to fabricate chemically converted G-CLS hierarchical architecture has been developed for the first time for this study. We demonstrated the G-CLS architecture based on the electrostatic attraction between CCG (negatively charged) and CLS (positively charged), which satisfactorily encapsulates electrochemically active CLS by graphene sheets. The approach resulted in high specific capacitance (1710.5 F g^{-1} at 1 A g^{-1} and 1477.6 F g^{-1} at 10 A g^{-1}) and outstanding cycling stability (77.9% retention after 8000 cycles). An asymmetric supercapacitor based on G-CLS and rGO as the positive and negative electrodes, respectively, in aqueous electrolyte was assembled. The ASC can be cycled reversibly in the high-voltage region of 0−1.4 V and exhibited a high energy density of 35.5 Wh kg^{-1} and a high power density of 5578.1 W kg^{-1}. Good rate capability and the robust long-term cycling stability were also achieved. We believe that the proposed hybrid structure strategy would facilitate the production of next-generation energy storage devices.

ASSOCIATED CONTENT

Supporting Information

Figure S1, SEM image of CLH; Figure S2, XPS survey spectra of CLS; Figure S3, High-resolution XPS spectrum of C 1s (a), O1s (b), Ni 2p (c), and Al 2p (d); Figure S4, Nitrogen adsorption-desorption isotherms of CLH, CLS and G-CLS, and pore size distribution (inset) of G-CLS; Figure S5, The relationship of (a) charge Q *vs* $v^{-1/2}$ and (b) Q^{-1} *vs* $v^{1/2}$; Figure S6, Discharge curves of CLH (a) and CLS (b) at various densities; Figure S7, A red LED powered by the tandem G-CLS//rGO; Table S1, Comparison of the

electrochemical performance of the reported LDHs and graphene based electrodes in recent three years and the present work; Table S2, Fittted values of R_s, R_{ct}, C *dl*, W, and C *ps* through CNLS fitting of the EIS based on the proposed equivalent circuit in figure 5e.

ACKNOWLEDGEMENT

This work was supported by the Global Frontier hybrid Interface Materials (GFHIM) program of the National Research Foundation of Korea (NRF) funded by the Ministry of Science, ICT & Future Planning (2013M3A6B1078874), the Science and Technology Development Fund from Macau SAR (FDCT-098/2015/A3), and the Start-up Research Grant (SRG2015-00057-FST) from Research & Development Office at University of Macau.

REFERENCES

(1) Narayanan, S.; Hajzus, J. R.; Treacy, C. E.; Bockstaller, M. R.; Porter, L. M., Polymer Embedded Silver-Nanowire Network Structures - A Platform for the Facile Fabrication of Flexible Transparent Conductors. *ECS J Solid State Sc* **2014,** *3* (11), 363-369.

(2)Yang, Y.; Li, L.; Ruan, G. D.; Fei, H. L.; Xiang, C. S.; Fan, X. J.; Tour, J. M., Hydrothermally Formed Three-Dimensional Nanoporous $Ni(OH)_2$ Thin-Film Supercapacitors. *Acs Nano* **2014,** *8* (9), 9622-9628.

(3)Fan, Z. J.; Yan, J.; Wei, T.; Zhi, L. J.; Ning, G. Q.; Li, T. Y.; Wei, F., Asymmetric Supercapacitors Based on Graphene/MnO_2 and Activated Carbon Nanofiber Electrodes with High Power and Energy Density. *Adv Funct Mater* **2011,** *21* (12), 2366-2375.

(4) Lu, X. H.; Yu, M. H.; Zhai, T.; Wang, G. M.; Xie, S. L.; Liu, T. Y.; Liang, C. L.; Tong, Y. X.; Li, Y., High Energy Density Asymmetric Quasi-Solid-State Supercapacitor Based on Porous Vanadium Nitride Nanowire Anode. *Nano Lett* **2013,** *13* (6), 2628-2633.

(5) Vialat, P.; Mousty, C.; Taviot-Gueho, C.; Renaudin, G.; Martinez, H.; Dupin, J. C.; Elkaim, E.; Leroux, F., High-Performing Monometallic Cobalt Layered Double Hydroxide Supercapacitor with Defined Local Structure. *Adv Funct Mater* **2014,** *24* (30), 4831-4842.

(6) Mignani, A.; Ballarin, B.; Giorgetti, M.; Scavetta, E.; Tonelli, D.; Boanini, E.; Prevot, V.; Mousty, C.; Iadecola, A., Heterostructure of Au Nanoparticles-NiAl Layered Double Hydroxide: Electrosynthesis, Characterization, and Electrocatalytic Properties. *J Phys Chem C* **2013,** *117* (31), 16221-16230.

(7) Wu, S. X.; Hui, K. S.; Hui, K. N., One-Dimensional Core-Shell Architecture Composed of Silver Nanowire@Hierarchical Nickel-Aluminum Layered Double Hydroxide Nanosheet as Advanced Electrode Materials for Pseudocapacitor. *J Phys Chem C* **2015,** *119* (41), 23358-23365.

(8) Wang, Q.; O'Hare, D., Recent Advances in the Synthesis and Application of Layered Double Hydroxide (LDH) Nanosheets. *Chem Rev* **2012,** *112* (7), 4124-4155.

(9) Wimalasiri, Y.; Fan, R.; Zhao, X. S.; Zou, L., Assembly of Ni-Al layered double hydroxide and graphene electrodes for supercapacitors. *Electrochim Acta* **2014,** *134*, 127-135.

(10) Liang, H. F.; Meng, F.; Caban-Acevedo, M.; Li, L. S.; Forticaux, A.; Xiu, L. C.; Wang, Z. C.; Jin, S., Hydrothermal Continuous Flow Synthesis and Exfoliation of NiCo Layered Double Hydroxide Nanosheets for Enhanced Oxygen Evolution Catalysis. *Nano Lett* **2015,** *15* (2), 1421-1427.

(11) Liu, M. K.; He, S. X.; Miao, Y. E.; Huang, Y. P.; Lu, H. Y.; Zhang, L. S.; Liu, T. X., Eco-friendly Synthesis of Hierarchical Ginkgo-derived Carbon Nanoparticles/NiAl-layered Double Hydroxide Hybrid Electrodes toward High-performance Supercapacitors. *Rsc Adv* **2015,** *5* (68), 55109-55118.

(12) Liu, X. X.; Wang, C.; Dou, Y. B.; Zhou, A. W.; Pan, T.; Han, J. B.; Wei, M., A NiAl Layered Double Hydroxide@Carbon Nanoparticles Hybrid Electrode for High-Performance Asymmetric Supercapacitors. *J Mater Chem A* **2014,** *2* (6), 1682-1685.

(13) He, F.; Hu, Z. B.; Liu, K. Y.; Zhang, S. R.; Liu, H. T.; Sang, S. B., In Situ Fabrication of Nickel Aluminum-Layered Double Hydroxide Nanosheets/Hollow Carbon

Nanofibers Composite as A Novel, Electrode Material for Supercapacitors. *J Power Sources* **2014,** *267*, 188-196.

(14) Zhao, J. W.; Chen, J.; Xu, S. M.; Shao, M. F.; Zhang, Q.; Wei, F.; Ma, J.; Wei, M.; Evans, D. G.; Duan, X., Hierarchical NiMn Layered Double Hydroxide/Carbon Nanotubes Architecture with Superb Energy Density for Flexible Supercapacitors. *Adv Funct Mater* **2014,** *24* (20), 2938-2946.

(15) Gao, Z.; Wang, J.; Li, Z. S.; Yang, W. L.; Wang, B.; Hou, M. J.; He, Y.; Liu, Q.; Mann, T.; Yang, P. P.; Zhang, M. L.; Liu, L. H., Graphene Nanosheet/Ni^{2+}/Al^{3+} Layered Double-Hydroxide Composite as a Novel Electrode for a Supercapacitor. *Chem Mater* **2011,** *23* (15), 3509-3516.

(16) Li, M.; Cheng, J. P.; Fang, J. H.; Yang, Y.; Liu, F.; Zhang, X. B., NiAl-layered Double Hydroxide/Reduced Graphene Oxide Composite: Microwave-assisted Synthesis and Supercapacitive Properties. *Electrochim Acta* **2014,** *134*, 309-318.

(17) Momodu, D.; Bello, A.; Dangbegnon, J.; Barzeger, F.; Fabiane, M.; Manyala, N., P3HT:PCBM/Nickel-Aluminum Layered Double Hydroxide-Graphene Foam Composites for Supercapacitor Electrodes. *J Solid State Electr* **2015,** *19* (2), 445-452.

(18) Ma, W.; Ma, R. Z.; Wang, C. X.; Liang, J. B.; Liu, X. H.; Zhou, K. C.; Sasaki, T., A Superlattice of Alternately Stacked Ni-Fe Hydroxide Nanosheets and Graphene for Efficient Splitting of Water. *Acs Nano* **2015,** *9* (2), 1977-1984.

(19) Yang, S. B.; Feng, X. L.; Wang, L.; Tang, K.; Maier, J.; Mullen, K., Graphene-Based Nanosheets with a Sandwich Structure. *Angew Chem Int Edit* **2010,** *49* (28), 4795-4799.

(20) Cao, Y.; Li, G.; Li, X., Graphene/Layered Double Hydroxide Nanocomposite: Properties, Synthesis, and Applications. *Chem Eng J* **2016,** *292*, 207-223.

(21)Zhong, Y.; Liao, Y.; Gao, A.; Hao, J.; Shu, D.; Huang, Y.; Zhong, J.; He, C.; Zeng, R., Supercapacitive Behavior of Electrostatic Self-Assembly Reduced Graphene Oxide/CoAl-Layered Double Hydroxides Nanocomposites. *J Alloy Compd* **2016,** *669*, 146-155.

(22) Bao, L. H.; Zang, J. F.; Li, X. D., Flexible Zn_2SnO_4/MnO_2 Core/Shell Nanocable-Carbon Microfiber Hybrid Composites for High-Performance Supercapacitor Electrodes. *Nano Lett* **2011,** *11* (3), 1215-1220.

(23) Hou, Y.; Cheng, Y. W.; Hobson, T.; Liu, J., Design and Synthesis of Hierarchical MnO_2 Nanospheres/Carbon Nanotubes/Conducting Polymer Ternary Composite for High Performance Electrochemical Electrodes. *Nano Lett* **2010,** *10* (7), 2727-2733.

(24) Yang, S. B.; Feng, X. L.; Ivanovici, S.; Mullen, K., Fabrication of Graphene-Encapsulated Oxide Nanoparticles: Towards High-Performance Anode Materials for Lithium Storage. *Angew Chem Int Edit* **2010,** *49* (45), 8408-8411.

(25) Wang, J. Z.; Zhong, C.; Wexler, D.; Idris, N. H.; Wang, Z. X.; Chen, L. Q.; Liu, H. K., Graphene-Encapsulated Fe_3O_4 Nanoparticles with 3D Laminated Structure as Superior Anode in Lithium Ion Batteries. *Chem-Eur J* **2011,** *17* (2), 661-667.

(26) Ji, X. Q.; Zhang, W. L.; Shan, L.; Tian, Y.; Liu, J. Q., Self-assembly preparation of SiO_2@Ni-Al layered double hydroxide composites and their enhanced electrorheological characteristics. *Sci Rep* **2015,** *5*.

(27) Hummers Jr W. S.; Offeman R. E., Preparation of Graphitic Oxide. *J. Am. Chem. Soc.* **1958,** *80*, 1339.

(28) Kovtyukhova, N. I.; Ollivier, P. J.; Martin, B. R.; Mallouk, T. E.; Chizhik, S. A.; Buzaneva, E. V.; Gorchinskiy, A. D., Layer-by-Layer Assembly of Ultrathin Composite Films from Micron-Sized Graphite Oxide Sheets and Polycations. *Chem Mater* **1999,** *11* (3), 771-778.

(29) Li, D.; Muller, M. B.; Gilje, S.; Kaner, R. B.; Wallace, G. G., Processable Aqueous Dispersions of Graphene Nanosheets. *Nat Nanotechnol* **2008,** *3* (2), 101-105.

(30) Sun, X. M.; Li, Y. D., Colloidal Carbon Spheres and Their Core/Shell Structures with Noble-Metal Nanoparticles. *Angew Chem Int Edit* **2004,** *43* (5), 597-601.

(31) Yang, S. B.; Gong, Y. J.; Liu, Z.; Zhan, L.; Hashim, D. P.; Ma, L. L.; Vajtai, R.; Ajayan, P. M., Bottom-up Approach toward Single-Crystalline VO_2-Graphene Ribbons as Cathodes for Ultrafast Lithium Storage. *Nano Lett* **2013,** *13* (4), 1596-1601.

(32) Mai, L. Q.; Minhas-Khan, A.; Tian, X. C.; Hercule, K. M.; Zhao, Y. L.; Lin, X.; Xu, X., Synergistic Interaction between Redox-Active Electrolyte and Binder-Free Functionalized Carbon for Ultrahigh Supercapacitor Performance. *Nat Commun* **2013,** *4*.

(33) Wu S. X.; Hui K. S.; Hui K. N.; Kim K. H., Ultrathin Porous NiO Nanoflake Arrays on Nickel Foam as An Advanced Electrode for High Performance Asymmetric Supercapacitors. *J Mater Chem A* **2016**, *4*, 4146-4152.

(34) Sun, X. F.; Qiu, X. Q.; Li, L. P.; Li, G. S., ZnO Twin-Cones: Synthesis, Photoluminescence, and Catalytic Decomposition of Ammonium Perchlorate. *Inorg Chem* **2008,** *47* (10), 4146-4152.

(35) Li, R. C.; Hu, Z. X.; Shao, X. F.; Cheng, P. P.; Li, S. S.; Yu, W. D.; Lin, W. R.; Yuan, D. S., Large Scale Synthesis of NiCo Layered Double Hydroxides for Superior Asymmetric Electrochemical Capacitor. *Sci Rep* **2016,** *6*,187137.

(36) Zhang, F. Z.; Guo, L.; Xu, S. L.; Zhang, R., Preparation of Nickel-Aluminum-Containing Layered Double Hydroxide Films by Secondary (Seeded) Growth Method and Their Electrochemical Properties. *Langmuir* **2015,** *31* (24), 6704-6712.

(37) Chen, H.; Hu, L. F.; Chen, M.; Yan, Y.; Wu, L. M., Nickel- Cobalt Layered Double Hydroxide Nanosheets for High- performance Supercapacitor Electrode Materials. *Adv Funct Mater* **2014,** *24* (7), 934-942.

(38) Patzke, G. R.; Zhou, Y.; Kontic, R.; Conrad, F., Oxide Nanomaterials: Synthetic Developments, Mechanistic Studies, and Technological Innovations. *Angew Chem Int Edit* **2011,** *50* (4), 826-859.

(39) Fan, L.; Tang, L.; Gong, H. F.; Yao, Z. H.; Guo, R., Carbon-Nanoparticles Encapsulated in Hollow Nickel Oxides for Supercapacitor Application. *J Mater Chem* **2012,** *22* (32), 16376-16381.

(40) Song, Y. C.; Wang, J.; Li, Z. S.; Guan, D. H.; Mann, T.; Liu, Q.; Zhang, M. L.; Liu, L. H., Self-Assembled Hierarchical Porous Layered Double Hydroxides by Solvothermal Method and Their Application for Capacitors. *Micropor Mesopor Mat* **2012,** *148* (1), 159-165.

(41) Gunawan, P.; Xu, R., Direct Assembly of Anisotropic Layered Double Hydroxide (LDH) Nanocrystals on Spherical Template for Fabrication of Drug-LDH Hollow Nanospheres. *Chem Mater* **2009,** *21* (5), 781-783.

(42) Lang, J. W.; Kong, L. B.; Liu, M.; Luo, Y. C.; Kang, L., $Co_{0.56}Ni_{0.44}$ Oxide Nanoflake Materials and Activated Carbon for Asymmetric Supercapacitor. *J Electrochem Soc* **2010,** *157* (12), A1341-A1346.

(43) Zhu, Y. Q.; Cao, C. B.; Tao, S.; Chu, W. S.; Wu, Z. Y.; Li, Y. D., Ultrathin Nickel Hydroxide and Oxide Nanosheets: Synthesis, Characterizations and Excellent Supercapacitor Performances. *Sci Rep* **2014,** *4*,5787.

(44) Ji, J. Y.; Zhang, L. L.; Ji, H. X.; Li, Y.; Zhao, X.; Bai, X.; Fan, X. B.; Zhang, F. B.; Ruoff, R. S., Nanoporous Ni(OH) Thin Film on 3D Ultrathin-Graphite Foam for Asymmetric Supercapacitor. *Acs Nano* **2013,** *7* (7), 6237-6243.

(45) Chen, J.; Sheng, K. X.; Luo, P. H.; Li, C.; Shi, G. Q., Graphene Hydrogels Deposited in Nickel Foams for High-Rate Electrochemical Capacitors. *Adv Mater* **2012,** *24* (33), 4569-4573.

(46) Ning, F. Y.; Shao, M. F.; Zhang, C. L.; Xu, S. M.; Wei, M.; Duan, X., Co_3O_4@Layered Double Hydroxide Core/Shell Hierarchical Nanowire Arrays for Enhanced Supercapacitance Performance. *Nano Energy* **2014,** *7*, 134-142.

(47) White, B.; Banerjee, S.; O'Brien, S.; Turro, N. J.; Herman, I. P., Zeta-Potential Measurements of Surfactant-Wrapped Individual Single-Walled Carbon Nanotubes. *J Phys Chem C* **2007,** *111* (37), 13684-13690.

(48) Pandey, D.; Reifenberger, R.; Piner, R., Scanning Probe Microscopy Study of Exfoliated Oxidized Graphene Sheets. *Surf Sci* **2008,** *602* (9), 1607-1613.

(49) Szabo, T.; Berkesi, O.; Forgo, P.; Josepovits, K.; Sanakis, Y.; Petridis, D.; Dekany, I., Evolution of Surface Functional Groups in A Series of Progressively Oxidized Graphite Oxides. *Chem Mater* **2006,** *18* (11), 2740-2749.

(50) Chen, Y. C.; Ishihara, H.; Chen, W. J.; DeMarco, N.; Siordia, A.; Sun, Y. S.; Lin, O.; Chu, C. W.; Tung, V. C., Capillarity-Assisted Electrostatic Assembly of Hierarchically

Functional 3D Graphene: TiO_2 Hybrid Photoanodes. *Adv Mater Interfaces* **2015,** *2* (17), 1500292.

(51) Guo, C. X.; Yang, H. B.; Sheng, Z. M.; Lu, Z. S.; Song, Q. L.; Li, C. M., Layered Graphene/Quantum Dots for Photovoltaic Devices. *Angew Chem Int Edit* **2010,** *49* (17), 3014-3017.

(52) Li, N.; Yang, G. Z.; Sun, Y.; Song, H. W.; Cui, H.; Yang, G. W.; Wang, C. X., Free-Standing and Transparent Graphene Membrane of Polyhedron Box-Shaped Basic Building Units Directly Grown Using a NaCl Template for Flexible Transparent and Stretchable Solid-State Supercapacitors. *Nano Lett* **2015,** *15* (5), 3195-3203.

(53) Graf, D.; Molitor, F.; Ensslin, K.; Stampfer, C.; Jungen, A.; Hierold, C.; Wirtz, L., Spatially Resolved Raman Spectroscopy of Single- and Few-Layer Graphene. *Nano Lett* **2007,** *7* (2), 238-242.

(54) Juan Yang, C. Y., Xiaoming Fan, Suxia Liang, Shaofeng Li, Huawei Huang, Zheng Ling, Ce Hao and Jieshan Qiu, Electroactive edge Site-Enriched Nickel–Cobalt Sulfide into Graphene Frameworks for High Performance Asymmetric Supercapacitors. *Energ Environ Sci* **2016**.

(55) Xu, J. M.; Zhang, J.; Wang, B. B.; Liu, F., Shape-Regulated Synthesis of Cobalt Oxide and Its Gas-Sensing Property. *J Alloy Compd* **2015,** *619*, 361-367.

(56) Wu, Q. D.; Gao, X. P.; Li, G. R.; Pan, G. L.; Yan, T. Y.; Zhu, H. Y., Microstructure and Electrochemical Properties of Al-Substituted Nickel Hydroxides Modified with CoOOH Nanoparticles. *J Phys Chem C* **2007,** *111* (45), 17082-17087.

(57) Nguyen, T.; Boudard, M.; Rapenne, L.; Carmezim, M. J.; Montemor, M. F., Morphological Changes and Electrochemical Response of Mixed Nickel Manganese Oxides as Charge Storage Electrodes. *J Mater Chem A* **2015,** *3* (20), 10875-10882.

(558) Nguyen, T.; Eugenio, S.; Boudard, M.; Rapenne, L.; Carmezim, M. J.; Silva, T. M.; Montemor, M. F., Hybrid Nickel Manganese Oxide Nanosheet-3D Metallic Dendrite Percolation Network Eectrodes for High-Rate Electrochemical Energy Storage. *Nanoscale* **2015,** *7* (29), 12452-12459.

(569) Ardizzone, S.; Fregonara, G.; Trasatti, S., Inner and Outer Active Surface of Ruo2 Electrodes. *Electrochim Acta* **1990,** *35* (1), 263-267.

(60) Wu, M. S.; Wang, M. J.; Jow, J. J., Fabrication of porous nickel oxide film with open macropores by electrophoresis and electrodeposition for electrochemical capacitors. *J Power Sources* **2010,** *195* (12), 3950-3955.

(61) Stoller, M. D.; Park, S. J.; Zhu, Y. W.; An, J. H.; Ruoff, R. S., Graphene-Based Ultracapacitors. *Nano Lett* **2008,** *8* (10), 3498-3502.

(62) Sun, G. Z.; Zhang, X.; Lin, R. Z.; Yang, J.; Zhang, H.; Chen, P., Hybrid Fibers Made of Molybdenum Disulfide, Reduced Graphene Oxide, and Multi-Walled Carbon Nanotubes for Solid-State, Flexible, Asymmetric Supercapacitors. *Angew Chem Int Edit* **2015,** *54* (15), 4651-4656.

(63) Yan, J.; Wang, Q.; Wei, T.; Fan, Z. J., Recent Advances in Design and Fabrication of Electrochemical Supercapacitors with High Energy Densities. *Adv Energy Mater* **2014,** *4* (4),1300816-1300858.

FIGURE CAPTIONS

Scheme 1. Schematic diagram of the G-CLS hybrid structure.

Figure 1. (a) Schematic illustration of the proposed CLS evolution process. (b) SEM images of CSs. (c) SEM images of CLS. (d) XRD patterns and (e) Raman spectrum of the CS, CLH, and CLS.

Figure 2. TEM (a, b, c, and d) and SAED (inset in b) pattern images of the CLS.

Figure 3. Zeta potential profiles of GO, CCG, and CLS before and after functionalization with CTAB.

Figure 4. (a, b) SEM images of G-CLS. (c) XRD pattern of the G-CLS and standard X-ray diffraction pattern. (d) Raman spectra of GO, CCG, and G-CLS.

Figure 5. Electrochemical performance of the supercapacitor samples: (a) CV curves of the CLH, CLS and G-CLS at a scan rate of 5 mV S^{-1}. (b) CV curves of G-CLS at different scans. (c) Galvanostatic charge–discharge profiles of G-CLS with different current densities. (d) Specific capacitances of CLH, CLS, and G-CLS at different current densities. (e) Nyquist plots of CLH, CLS, and G-CLS. (f) Cycling stability performance of CLH, CLS, and G-CLS.

Figure 6. (a) Schematic illustration of ASC cell containing G-CLS and rGO as the positive and negative electrodes, respectively. (b) Galvanostatic charge–discharge of G-CLS//rGO with the increase of potential window. (c) Coulombic efficiency and specific capacitance of G-CLS//rGO in 6 M KOH electrolyte versus different cell voltages.

Figure 7. Electrochemical performance of the G-CLS//rGO. (a) CV curves. (b) Galvanostatic charge–discharge curves. (c) Specific capacitances at different current densities. (d) Ragone plot. (e) Cycling performance and Coulombic efficiency.

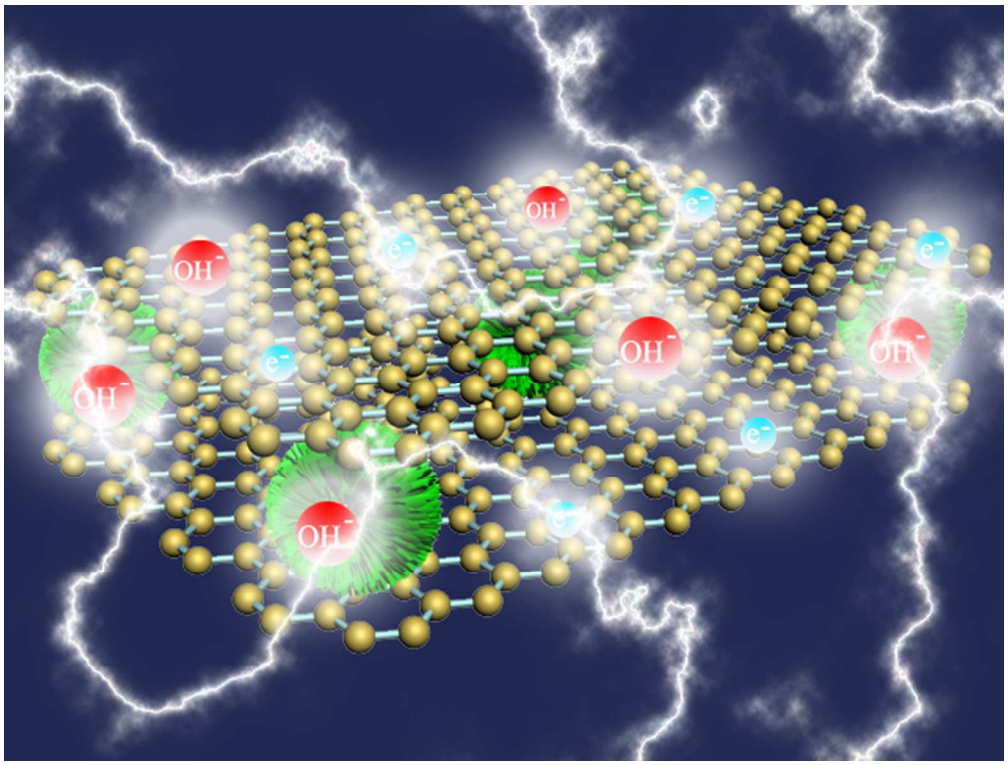

Graphic Abstract

177x134mm (300 x 300 DPI)

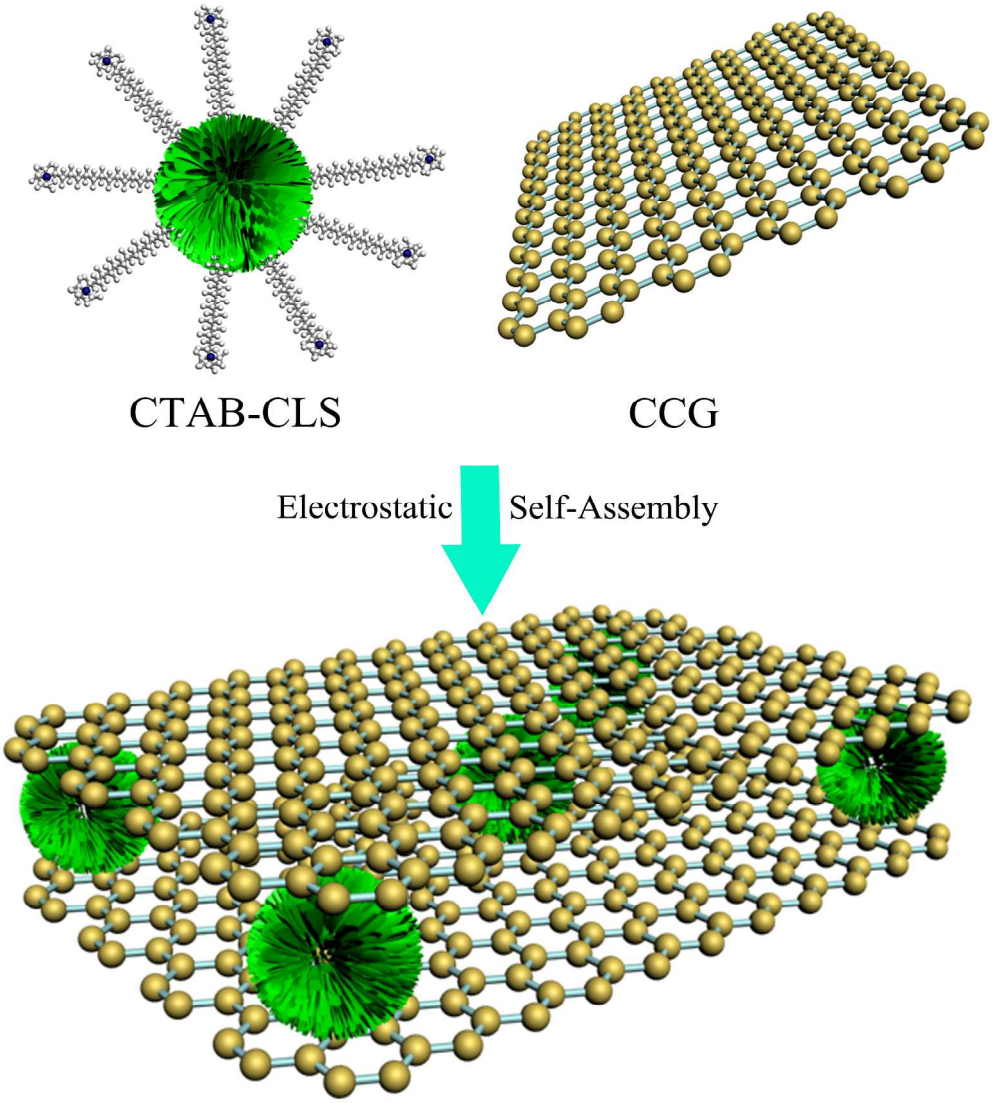

Scheme 1. Schematic diagram of the G-CLS hybrid structure.

154x170mm (600 x 600 DPI)

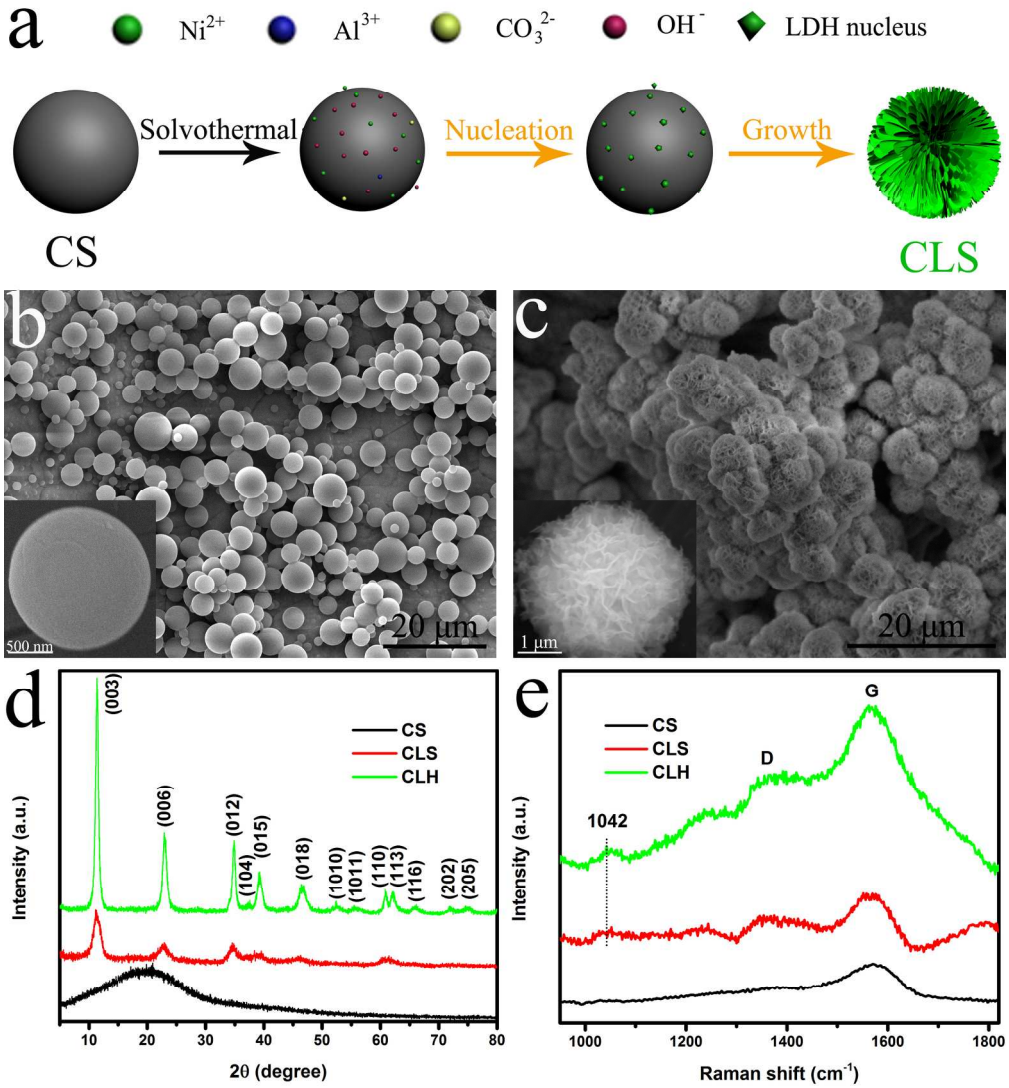

Figure 1. (a) Schematic illustration of the proposed CLS evolution process. (b) SEM images of CSs. (c) SEM images of CLS. (d) XRD patterns and (e) Raman spectrum of the CS, CLH, and CLS.

194x212mm (300 x 300 DPI)

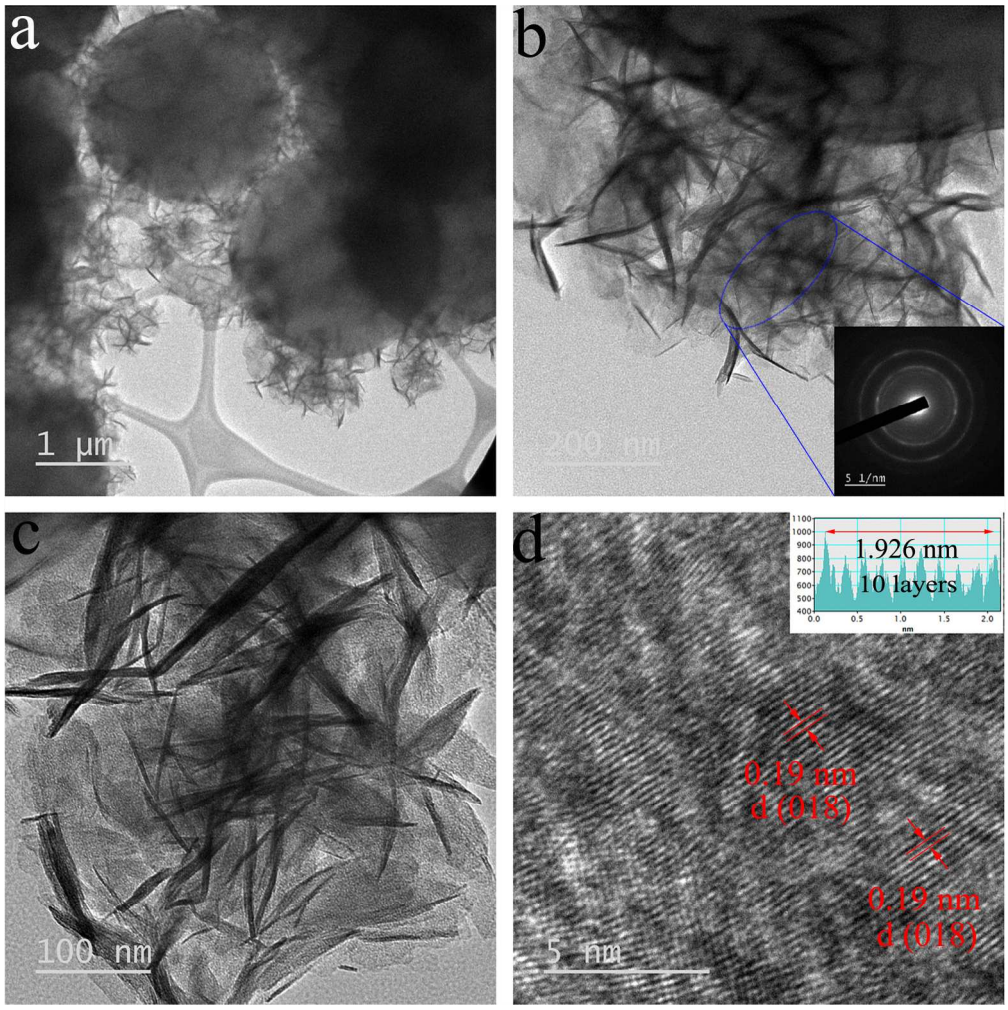

Figure 2. TEM and SAED pattern images of the CLS.

178x178mm (300 x 300 DPI)

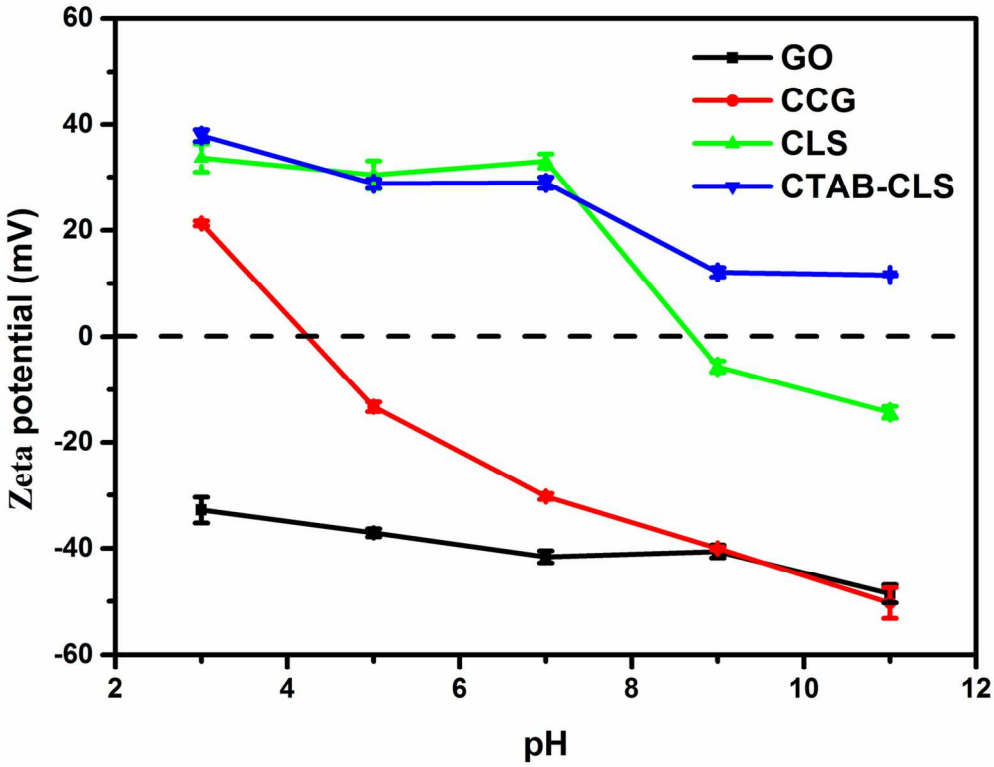

Figure 3. Zeta potential profiles of GO, CCG, and CLS before and after functionalization with CTAB.

65x50mm (600 x 600 DPI)

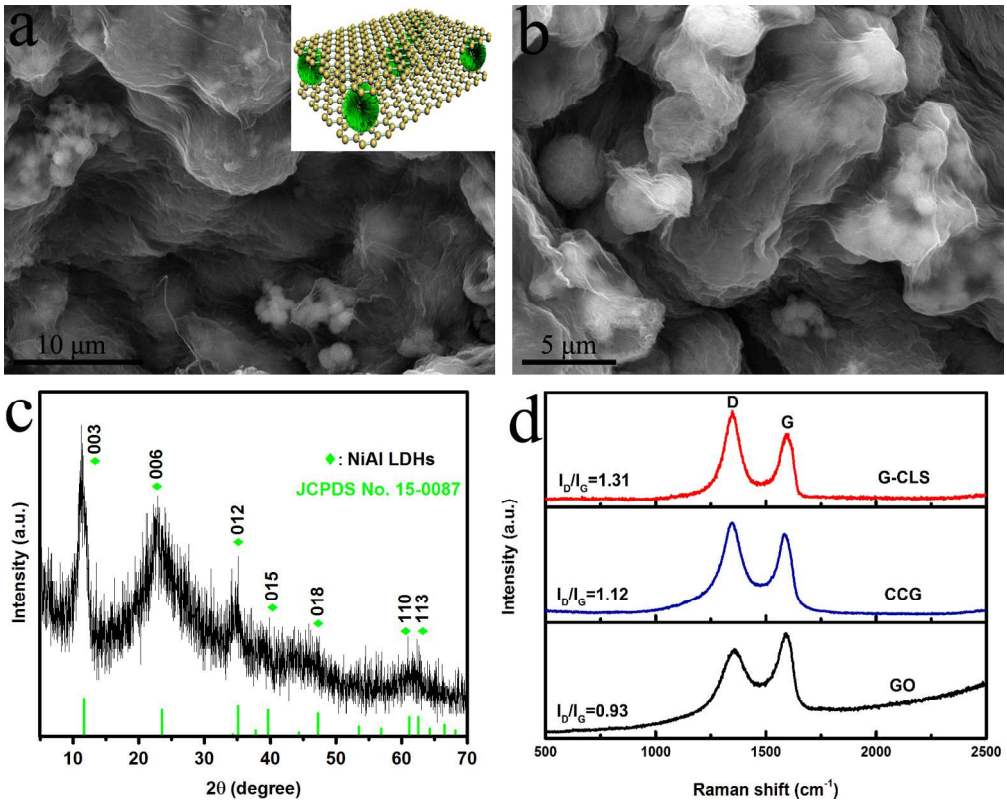

Figure 4. (a, b) SEM images of G-CLS. (c) XRD pattern of the G-CLS and standard X-ray diffraction pattern. (d) Raman spectra of GO, CCG, and G-CLS.

177x140mm (300 x 300 DPI)

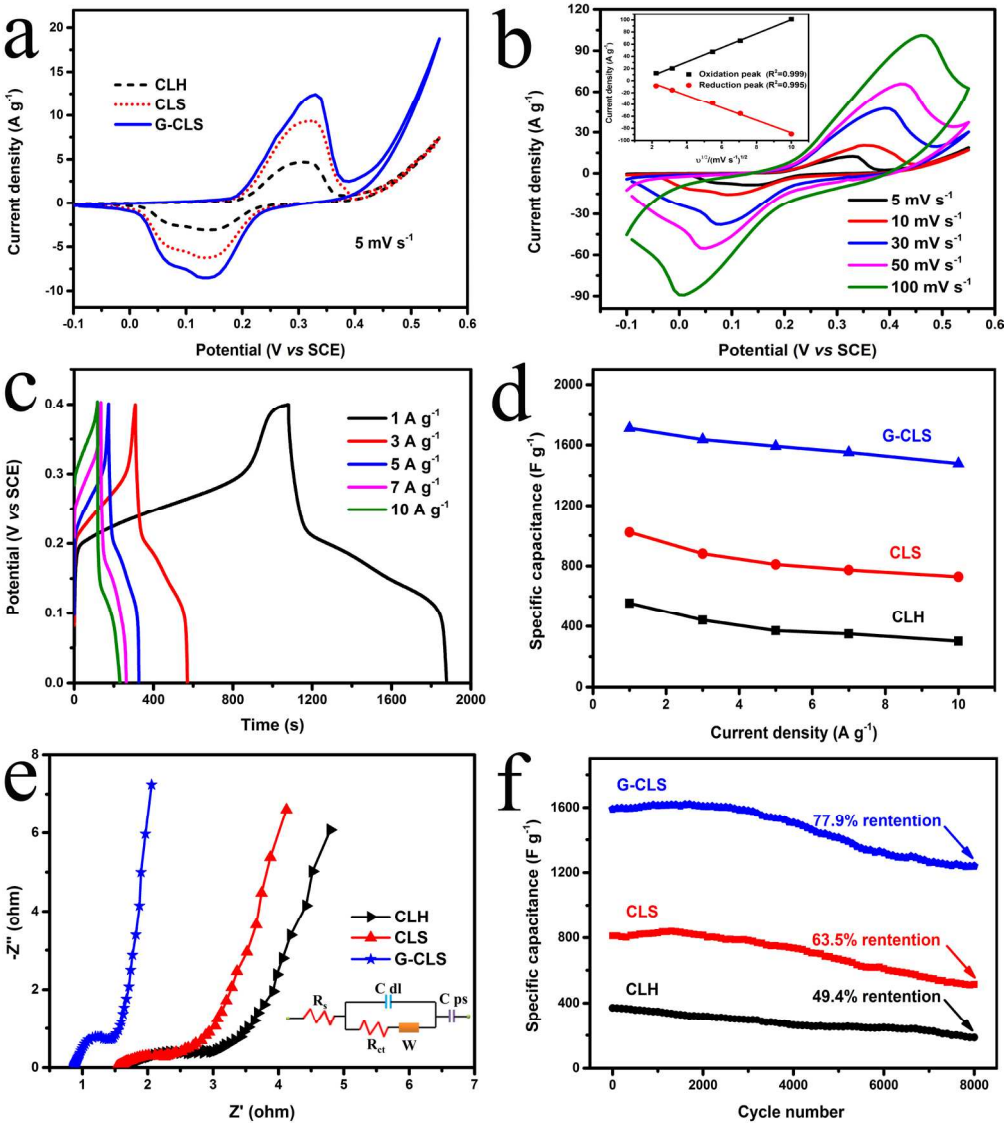

Figure 5. Electrochemical performance of the supercapacitor samples: (a) CV curves of the CLH, CLS and G-CLS at a scan rate of 5 mV S−1. (b) CV curves of G-CLS at different scans. (c) Galvanostatic charge–discharge profiles of G-CLS with different current densities. (d) Specific capacitances of CLH, CLS, and G-CLS at different current densities. (e) Nyquist plots of CLH, CLS, and G-CLS. (f) Cycling stability performance of CLH, CLS, and G-CLS.

177x199mm (300 x 300 DPI)

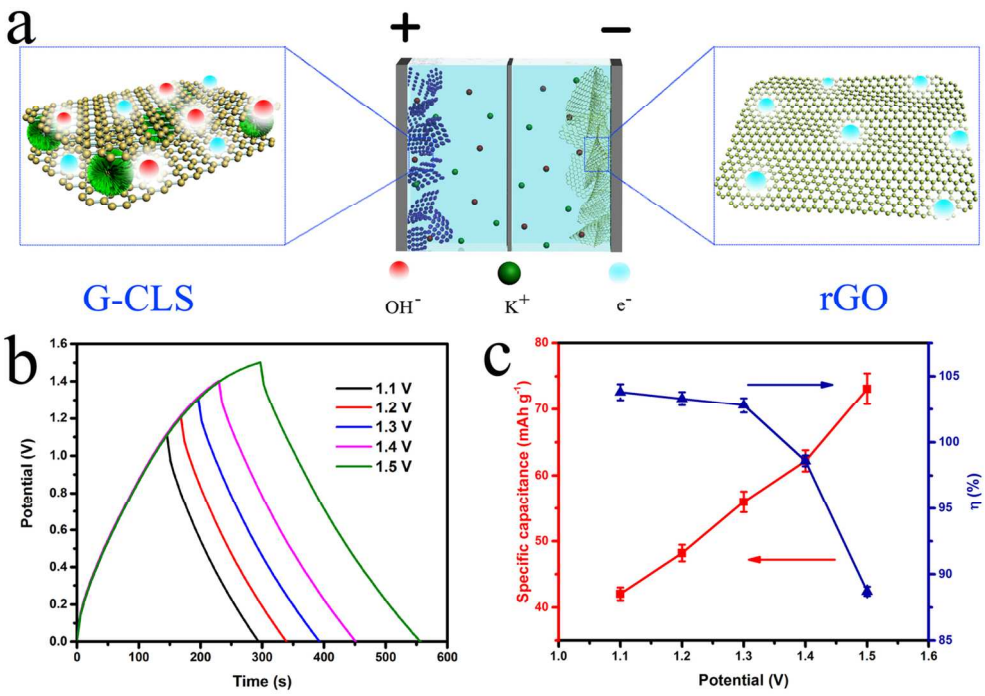

Figure 6. (a) Schematic illustration of ASC cell containing G-CLS and rGO as the positive and negative electrodes, respectively. (b) Galvanostatic charge–discharge of G-CLS//rGO with the increase of potential window. (c) Coulombic efficiency and specific capacitance of G-CLS//rGO in 6 M KOH electrolyte versus different cell voltages.

122x84mm (300 x 300 DPI)

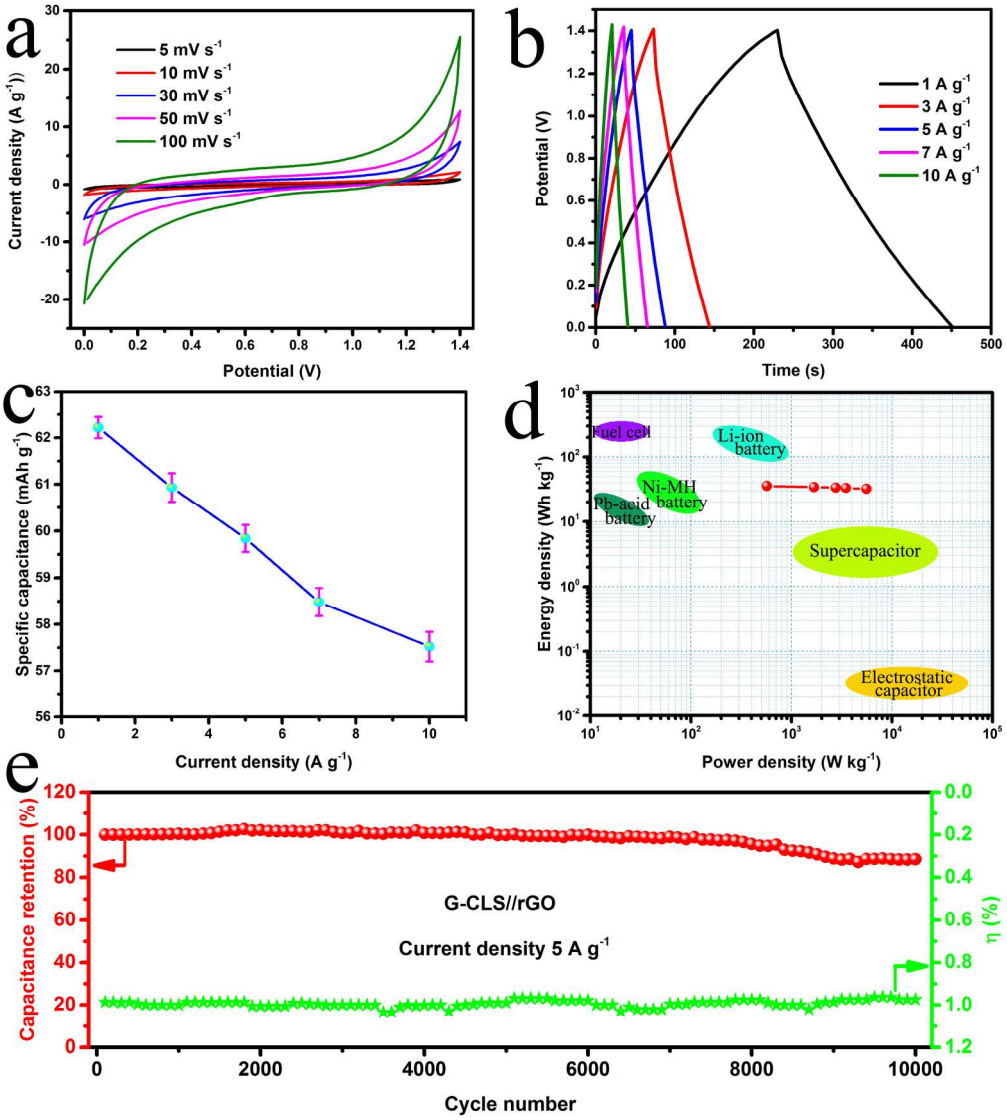

Figure 7. Electrochemical performance of the G-CLS//rGO. (a) CV curves. (b) Galvanostatic charge–discharge curves. (c) Specific capacitances at different current densities. (d) Ragone plot. (e) Cycling performance and Coulombic efficiency.

199x224mm (300 x 300 DPI)